



RESEARCH ARTICLE

Bifunctional nanoparticles decorated $\text{Ni}_{1-x}\text{Mn}_x\text{Co}_2\text{O}_4$ ultrathin nanoflakes-like electrodes for supercapacitor and overall water splitting

Surendra K. Shinde¹  | Swapnil S. Karade² | Nagesh C. Maile³  | Hemraj M. Yadav^{1,4} | Ajay D. Jagadale⁵ | Monali B. Jalak⁶ | Dae-Young Kim¹

¹Department of Biological and Environmental Science, College of Life Science and Biotechnology, Dongguk University-Seoul, Goyang-si, Gyeonggi-do, South Korea

²Department of Green Technology, University of Southern Denmark, Odense M, Denmark

³Department of Environmental Engineering, Kyungpook National University, Daegu, South Korea

⁴School of Nanoscience and Biotechnology, Shivaji University, Kolhapur, Maharashtra, India

⁵Center for Energy Storage and Conversion, School of Electrical & Electronics Engineering, SASTRA Deemed University, Thanjavur, India

⁶Department of Physics, Shivaji University, Kolhapur, India

Correspondence

Surendra K. Shinde and Dae-Young Kim,
Department of Biological and
Environmental Science, College of Life
Science and Biotechnology, Dongguk
University-Seoul, Biomedical Campus,
32 Dongguk-ro, Ilsandong-gu, Siksa-dong,
Goyang-si, Gyeonggi-do 10326,
South Korea.

Email: surendrashinde@dongguk.edu and
sbpkim@dongguk.edu

Funding information

Department of Science & Technology;
Dongguk University, Seoul, and Korea
Research Fund

Summary

Synthesizing triple transition metal oxide (TTMO) is an extraordinary strategy to develop electrodes for efficient energy storage and conversion devices, owing to their unique nanostructure with high porosity and specific surface area. The cobalt-based mixed-valence oxides have attracted great attention due to their facile synthesis, low cost, and excellent electrochemical performance. However, less attention is paid to investigating the effect of different substitutions on the physico-chemical properties of TTMO. In this study, nanoparticles (NPs) decorated ultrathin $\text{Ni}_{1-x}\text{Mn}_x\text{Co}_2\text{O}_4$ nanoflakes (NPs@NFs) are synthesized by tuning the molar ratio between Mn and Ni via facile deep eutectic solvents (DESS) method. Unique and highly porous NPs@NFs nanostructures aid to increase the overall surface area of the materials, whereas Mn, Ni, and Co ions participate in their redox-active capacity, improving the electrochemical activity of the material. This $\text{Ni}_{0.8}\text{Mn}_{0.2}\text{Co}_2\text{O}_4$ hybrid nanostructure exhibited excellent supercapacitive performance with a high specific capacity (Cs) of 761 mAh g^{-1} at a higher current density of 30 mA cm^{-2} and superior cycling retention of 92.86% after 10 000 cycles. Further, a hybrid asymmetric supercapacitor ($\text{Ni}_{0.8}\text{Mn}_{0.2}\text{Co}_2\text{O}_4/\text{AC}$) device exhibited an extended potential window of 1.5 V, which results in an ultrahigh energy density of 66.2 W kg^{-1} by sustaining a power density of 1519 Wh kg^{-1} . The electrocatalytic activity of the optimized $\text{Ni}_{0.8}\text{Mn}_{0.2}\text{Co}_2\text{O}_4$ shows the outstanding performance toward hydrogen evolution reaction (HER) ($150 \text{ mV}/161 \text{ mV dec}^{-1}$) and oxygen evolution reaction (OER) ($123 \text{ mV}/47 \text{ mV dec}^{-1}$) with a lower voltage of 1.51 V ($@10 \text{ mA cm}^{-2}$) for overall water splitting, with outstanding stability up to 25 hours. These results indicate that chemically synthesized ultrathin

NPs@NFs-like nanostructure is a capable electrode for multiple applications, such as supercapacitors, and overall water splitting.

Highlights

- Facial synthesis of nanoflakes of $\text{Ni}_{1-x}\text{Mn}_x\text{Co}_2\text{O}_4$ thin films by a DES method.
- Fully decorated NPs on the interconnected NFs provided a higher surface area.
- Nanostructures with a maximum specific capacity of 761 mAh g^{-1} at 30 mA cm^{-2} , with excellent stability of 92.86%.
- The solid-state device shows an excellent energy density of 66.2 Wh kg^{-1} at a power density of 1519 W kg^{-1} .
- The assembled $\text{Ni}_{0.8}\text{Mn}_{0.2}\text{Co}_2\text{O}_4$ /Ni-based water splitting exhibited low voltage (1.51 V) and superb stability up to 25 hours.

KEYWORDS

hydrogen evolution reaction, nanostructures, $\text{Ni}_{1-x}\text{Mn}_x\text{Co}_2\text{O}_4$, overall water splitting, oxygen evolution reaction, solid-state hybrid supercapacitors

1 | INTRODUCTION

Recently, various electrical devices, such as capacitors, supercapacitors, batteries, and fuel cells have emerged as energy storage devices in the electronic market. Consequently, various processes have been investigated to improve the electrical properties and develop nanomaterials for energy storage devices.¹⁻³ In particular, the Li-ion battery has been awarded a Noble Prize owing to its attractive energy storage capability as highlighted by the science community.¹ A previous study reported that Li-ion batteries provide a high energy density. However, their low power density has limited their effective application.² To address this limitation, supercapacitors, provide a significant energy density and a higher power density than ordinary capacitors.³ Based on their charge storage mechanism, supercapacitors are mainly divided into electric double-layer capacitors (EDLC) and pseudocapacitors.⁴ Various carbon-based materials, such as graphene (G), graphene oxides (GO), reduced-graphene oxides (RGO), activated carbon (AC), and carbon nanotubes (CNTs) have been applied as electrode materials in EDLC. In contrast, inorganic materials, such as metal oxides, metal chalcogenides, and conducting polymers, are used in pseudocapacitors.⁵ In the last few years, numerous researchers have devoted efforts to improving the materials used in pseudocapacitors because of their good conductivity, high redox-active sites, and superior electrical stability.⁶ Traditionally, metal oxides, such as RuO_2 , MnO_2 , NiO , and Co_3O_4 , are used as electrode materials in pseudocapacitors owing to their excellent

redox-active properties and good electrochemical response in terms of their high specific capacity and energy density.⁷⁻¹⁰ Currently, researchers are focusing on improving the performance of electrode materials. For example, previous studies have reported the enhanced electrochemical properties of various composites, hybrid, and core-shell heterostructure materials as electrode materials.

To date, various metal oxides with stable electrochemical performance have been reported for supercapacitors and overall water splitting applications. Previous studies have focused on improving the performance of these materials. Accordingly, different methods, materials, and composites have been developed to tune the morphological, nano size, and structural properties of electrode materials to enhance their electrical properties. For example, Sankapal et al.¹⁰ fabricated a Co_3O_4 /MWCNTs composite material with enhanced electrochemical performance. In addition, Shelke et al.¹¹ fabricated CoO-rGO thin film using the SILAR method. The fabricated CoO-rGO composite exhibited superior electrochemical properties and promising potential as a redox-active electrode. A previous study reported that electrode materials fabricated from multi-metal oxides formed by the combination of two metal ions exhibited significantly enhanced performance, which improved their redox activity and electronic conductivity.¹² For example, mixed TMOs, such as MnCo_2O_4 ,¹³ NiCo_2O_4 ,¹⁴ ZnCo_2O_4 ,¹⁵ and RuCo_2O_4 ,^{16,17} exhibit improved properties and have been used to develop high-energy supercapacitors electrodes. Pettong et al.¹³ fabricated MnCo_2O_4 nanofibers

(NF) as a superior battery-type electrode, and the electrode exhibited a high specific capacity of 123 mAh g⁻¹. Further, an asymmetric supercapacitor was fabricated using the synthesized MnCo₂O₄ NF and N-doped RGO as the positive and negative electrodes, respectively, and the supercapacitor exhibited an ultrahigh energy density of 54 Wh kg⁻¹ with stable cyclic stability of 85% after 3000 cycles. Dubal et al.¹⁴ summarized the synthesis and morphological, and electrochemical properties of NiCo₂O₄ in their review and discussed the importance of mixed metal oxides for supercapacitor application. Further, Raut et al.¹⁵ reported a simple and scalable chemical route for the synthesis of ZnCo₂O₄, and its composite with MWCNTs. They found that the overall capacity of the ZnCo₂O₄/MWCNTs composite electrode was two times higher than that of the pristine ZnCo₂O₄. Recently, a multi-metal oxide material (ie, RuCo₂O₄) was successfully synthesized using electrodeposition and the DES assistant co-precipitation method.^{16,17} The DES is a simple and supportive medium for the synthesis of nanomaterials owing to its attractive features, such as low cost, easy preparation, biodegradability, eco-friendliness, and versatility as it contains a diverse number of cation and anion species, which makes it a suitable solvent.¹⁸ To date, most researchers have developed binary metal oxides to fabricate supercapacitor electrodes with improved performance. However, developing mixed multi-metal oxide is a challenging task as it is very difficult to obtain the pure phase. Tamboli et al.¹⁹ successfully synthesized Mn-substituted NiCo₂O₄ using the hydrothermal method for supercapacitor application.

In this study, we successfully synthesized a mixed multi-metal valence, Ni_{1-x}Mn_xCo₂O₄ using a low-temperature DES method with different ratios of Ni and Mn ions for multiple applications including supercapacitors, and overall water splitting. The results revealed that the surface morphology, electrical conductivity, and electrochemical performance of the material improved with an increase in the Ni and Mn concentrations. In addition, among the thin films, Ni_{0.8}Mn_{0.2}Co₂O₄ films exhibited the highest electrochemical performance with a high Cs of 761 mAh g⁻¹. Further, a hybrid supercapacitor (Ni_{0.8}Mn_{0.2}Co₂O₄/AC) device demonstrated an ultrahigh energy density of 66.2 Wh kg⁻¹, powder density of 1519 W kg⁻¹, and superior long-term cyclic stability of 96% after 5000 cycles, respectively. Moreover, as an electrocatalyst, the Ni_{0.8}Mn_{0.2}Co₂O₄ showed improved electrocatalytic activity with appreciative values of overpotential and Tafel slope for HER (150 mV/161 mV dec⁻¹) and OER (123 mV/47 mV dec⁻¹) activities, which were quite impressive when compared with NiCo₂O₄ and MnCo₂O₄ electrodes. The assembled water-splitting cell (Ni_{0.8}Mn_{0.2}Co₂O₄/Ni//Ni_{0.8}Mn_{0.2}Co₂O₄/Ni) offered a lower

voltage of 1.51 V at a current density of 10 mA cm⁻² with excellent stability up to 25 hours.

2 | EXPERIMENTAL DETAILS

2.1 | Materials

Analytical-grade chemicals, including choline chloride, urea, nickel nitrate hexahydrate Ni(NO₃)₂·6H₂O, manganese (II) nitrate hydrate (Mn(NO₃)₂·H₂O), and cobalt nitrate hexahydrate (Co(NO₃)₂·6H₂O) were purchased from Sigma Aldrich and used directly without further purification.

2.2 | Synthesis of Ni_{1-x}Mn_xCo₂O₄

To prepare Ni_{1-x}Mn_xCo₂O₄, 1 g of Ni(NO₃)₂·6H₂O, 1 g of Mn(NO₃)₂·H₂O, and 2 g of Co(NO₃)₂·3H₂O were dissolved in a solution bath containing 10 mL DES, and the mixture was vigorously stirred for 30 minutes. Subsequently, 10 mL of double distilled water was added to the mixture dropwise, and the mixture was continuously stirred at room temperature (25°C) for 12 hours to complete the reaction. Thereafter, the conical flask was naturally cooled at room temperature and washed with double distilled water several times to remove other impurities. Lastly, the obtained product was filtered using a water vacuum filter to obtain a very fine powder. In addition, various Ni_{1-x}Mn_xCo₂O₄ thin films with varying Mn and Ni ratios (X = 0, 0.2, 0.4, 0.6, 0.8, and 1) were prepared using the same method, after which the samples were dried at 90°C for 12 hours. The as-prepared Ni_{1-x}Mn_xCo₂O₄ powders with a 2.5 mg cm⁻² active mass were used to prepare thin films on Ni foam using the drop coating method. After the preparation of the Ni_{1-x}Mn_xCo₂O₄ thin films were air-dried at room temperature. Furthermore, annealed these thin films were at 100°C for 30 minutes to vaporize the polyvinylidene difluoride binder, and then thin films were used further investigated. The as-prepared Ni_{1-x}Mn_xCo₂O₄ (X = 0, 0.2, 0.4, 0.6, 0.8, 1) thin films are hereafter denoted as NCO, NMCO4, NMCO3, NMCO2, NMCO1, and MCO, respectively.

3 | RESULTS AND DISCUSSION

3.1 | Surface morphological studies

The surface morphology of the Ni_{1-x}Mn_xCo₂O₄ hetero nanostructures affected the electrochemical performance

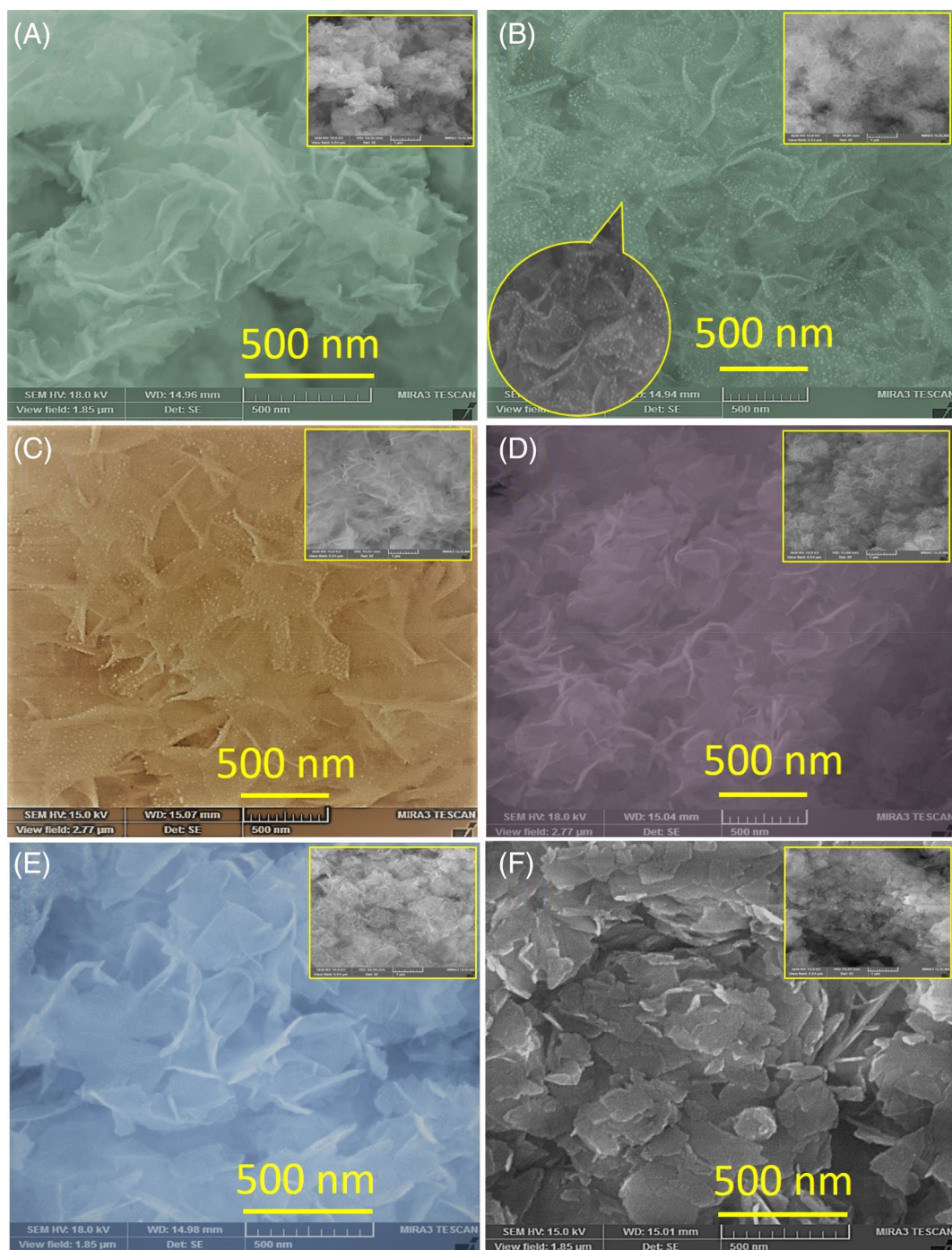


FIGURE 1 (A–F) FE-SEM images of the NCO, NMCO4, NMCO3, NMCO2, NMCO1, and MCO composite thin films and the inset show the high magnifications, respectively.

of the prepared electrodes. The surface morphology of the prepared NCO, NMCO4, NMCO3, NMCO2, NMCO1, and MCO thin films were investigated using FE-SEM, as shown in Figure 1A–F. The FE-SEM images revealed that the thin films exhibited a uniform and homogeneous NFs-like nanostructure growth with a porous surface and sharp vertical-edged highly porous NFs.^{20–22} Figure 1A shows the FE-SEM images of the interconnected chain of

the nanoflower-like nanostructures of NCO thin film. At high magnification (as shown in the inset of Figure 1A), the NFs with an average length and thickness of 200 to 300 and 25 to 35 nm, respectively, were interconnected to each other on a highly porous surface area. Furthermore, with a further increase in the quantity of Mn ($X = 0.2$), the surface of the NMCO4 NFs was fully decorated with heteronanostructured NPs (Figure 1B) on the porous and

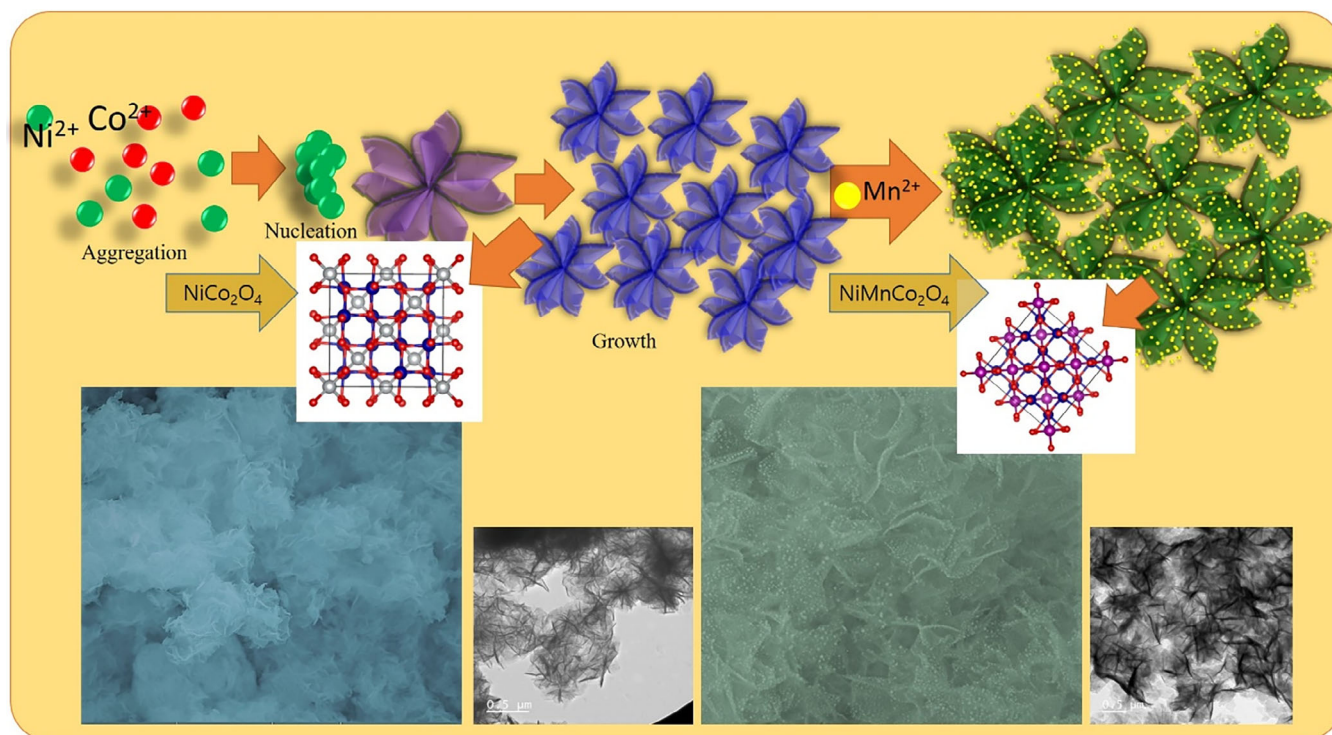


FIGURE 2 Schematic presentation of the formation of $\text{Ni}_{1-x}\text{Mn}_x\text{Co}_2\text{O}_4$ composite thin films

interconnected NFs.²³ The FE-SEM images revealed that the surface of the NFs was fully decorated with spherical NPs, as shown in the marked area. The porosity of the NMCO4 NFs was comparatively higher than that of the NCO thin film. In addition, the number of spherical NPs on the NFs was higher than in the NMCO3 thin film (Figure 1C), indicating an increase in the growth of MnCo_2O_4 particles on the backbone of the NiCo_2O_4 interconnected nanoflakes.^{24,25} The thickness of the NFs and the diameter of the NPs on the NMCO4 nanoflakes were approximately 5 to 7 nm and 15 to 20 nm, respectively. This decoration of the NPs on the heteronanostructured NFs enhanced the electrochemical performance of the NMCO4 electrode. This can be attributed to the highly porous and flexible interconnected network of the NMCO4, which enhanced the specific surface area and provided an easy pathway for ion/electron transfer during the electrochemical reaction.^{25,26} In addition, the surface of NMCO3 NFs was decorated with some NPs (Figure 1C), but at clear observation, NFs are not fully covered by NPs. At a higher magnification, smooth and porous NPs (<10 nm) were observed on the surface of the NMCO3 heterostructure. After the addition of Mn ($X = 0.6$) to the NiCo_2O_4 , the nanoflowers of the NMCO2 nanostructures developed on the surface of the nanomaterial, and the nanoflowers became interconnected to form nanoflakes-like nanostructures (as shown in Figure 1D). With a further increase Mn ($X = 0.8$) ratio in

NiCo_2O_4 , the surface morphology of the NMCO1 hetero nanostructures was fully decorated with nanoflakes, and the interconnected space between two vertical nanoflakes increased, which enhanced the electrochemical performance of the sample (Figure 1E).²³ Compared to the other samples, the surface morphology of the NMCO4 was significantly developed (Figure 1B). In contrast, a compact nanosheet (NSs) with an individual thickness of approximately 40 to 50 nm was observed on the surface of the MCO (Figure 1F). The surface morphology analysis indicates that the decoration of the 3D NFs-like nanostructure with hybrid 1D NPs enhanced the ion/electron transfer between two electrodes. The hetero nanostructures of the samples provided an easy pathway for the completion of Faradaic redox reactions, as well as enhanced the electrochemical activity of the $\text{Ni}_{1-x}\text{Mn}_x\text{Co}_2\text{O}_4$ hetero nanostructures.²⁵⁻²⁷

The possible growth mechanism of the $\text{Ni}_{1-x}\text{Mn}_x\text{Co}_2\text{O}_4$ nanostructures is shown in Figure 2. The preparation of the nanomaterials depended on the development of a solid phase from the supersaturated solution of Ni, Mn, and Co ions, which reacted with $(\text{OH})_2$ ions presented in water. Four major steps, including aggregation, nucleation, coalescence, and growth of nanomaterials, were involved in the synthesis of the nanostructures. In the first step, a heterogeneous reaction occurred between Ni, Co, and Mn to form clusters of the nanomaterials, and in the second step, the nanoparticles (NPs)

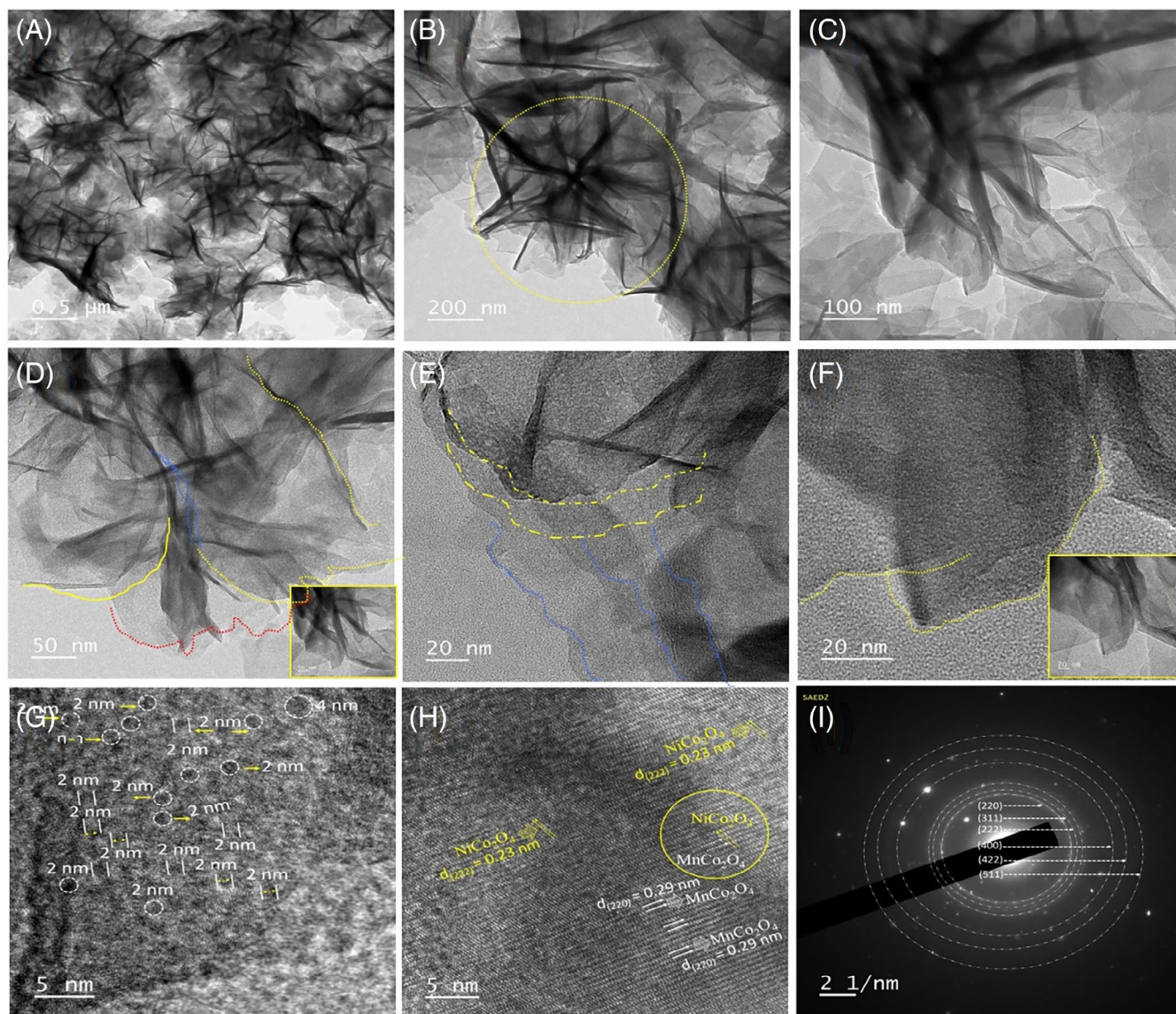


FIGURE 3 (A–H) TEM and HR-TEM images with low and high magnifications, (I) SAED patterns of the $\text{Ni}_{0.8}\text{Mn}_{0.2}\text{Co}_2\text{O}_4$ composite thin films

aggregated in the center of nucleation of the nanomaterials. The third and last steps involved the coalescence and initial growth of the nanostructure, respectively. In the third step, the NPs of the nanomaterials aggregated together, after which the binding of the nanostructures was initiated. In the last step, the nanostructures started to grow on the surface of thin films. This growth of the thin films was based on an ion-by-ion mechanism, which was associated with the ion-by-ion formation of the nanostructure on the surfaces of the thin films.^{9,14}

To further investigate the surface morphology of the as-prepared NCO, NMCO4, and MCO samples, the elemental composition of the thin films was investigated using TEM, high-resolution (HR)-TEM, EDS, and elemental mapping. Figure S1a–e shows the typical TEM

images of the NiCo_2O_4 thin film. Highly porous nanoflowers with a diameter of 300 to 400 nm were observed in the high and low-magnification images of NiCo_2O_4 thin film with a yellow marking area (Figure S1a). In addition, interconnected NFs with a thickness and length of 10 to 15 nm and 125 to 150 nm, respectively, were observed in the high-magnification images of the NiCo_2O_4 thin film (as shown in the marked area of Figure S1d,e). The highly porous NFs improved the specific surface area of NiCo_2O_4 thin film, which increased its ion/electron transfer rate, thus enhancing its electrochemical performance.^{26,27} The elemental mapping results revealed that the ternary NiCo_2O_4 thin film was uniformly covered with Ni, Co, and O elements, as shown in Figure S1f–i. In addition, the EDS analysis

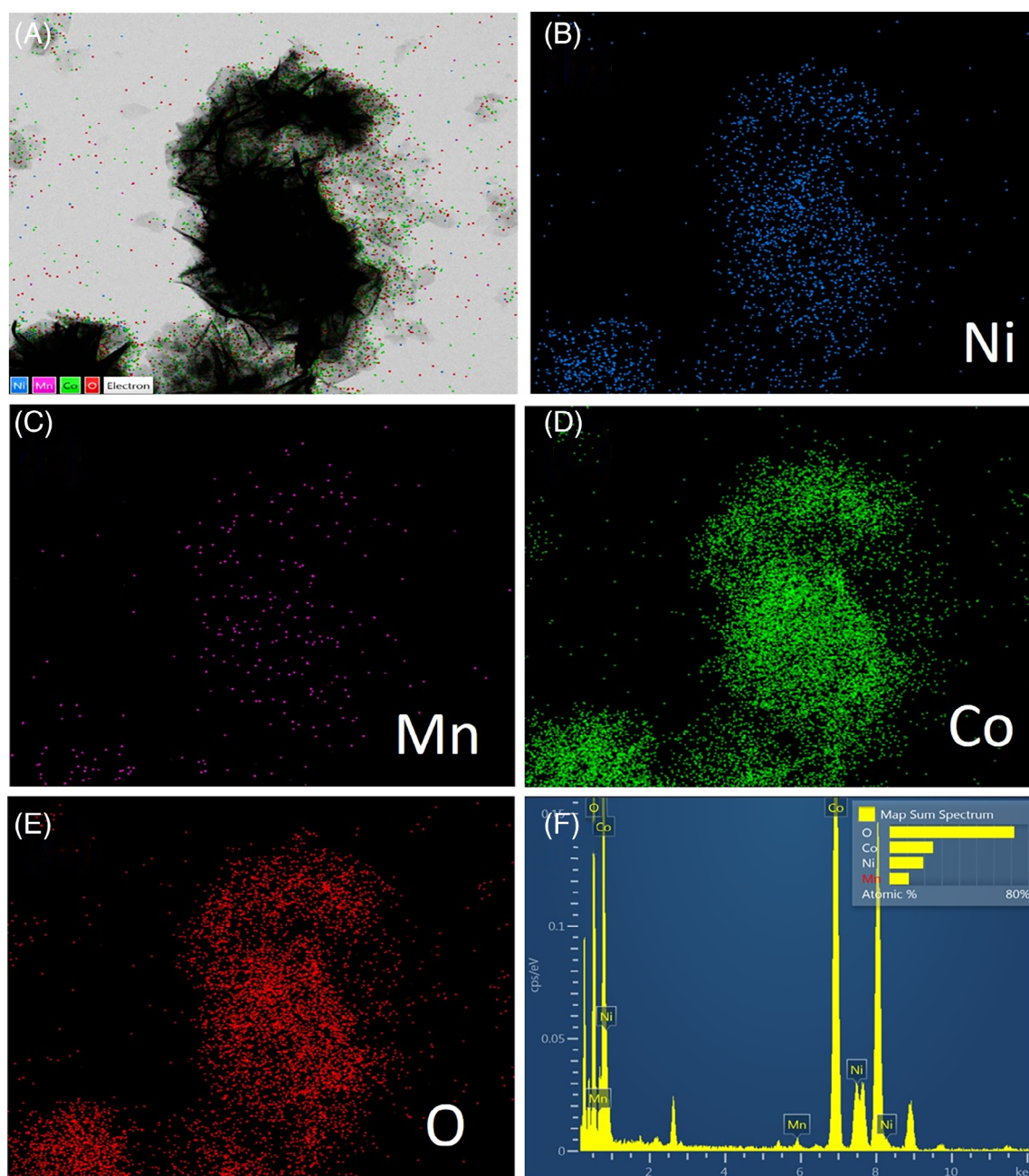


FIGURE 4 (A-E) Elemental mapping, (F) EDS of the $\text{Ni}_{0.8}\text{Mn}_{0.2}\text{Co}_2\text{O}_4$ composite thin films

confirmed the successful formation of the ternary NiCo_2O_4 phase (Figure S2). Furthermore, the EDS analysis revealed that the atomic weight percentage of the Ni, Co, and O elements was 16.67, 37.85, and 45.48%, respectively. The TEM images revealed that the surface of MnCo_2O_4 was fully and uniformly developed with hexagonal nanoplate-like nanostructures, as shown in Figure S3a,b. The elemental mapping and EDS results of the MnCo_2O_4 thin film are shown in Figures S3c-f and S3g. The mapping results revealed that Mn, Co, and O elements were homogeneously distributed on the surface of the MnCo_2O_4 thin film. The EDS pattern of MnCo_2O_4

thin film was consistent with its elemental mapping results. The EDS results revealed that the atomic weight percentage of Mn, Co, and O elements on the MCO sample was 30.36, 34.66, and 34.98%, respectively, indicating the successful formation of the ternary MnCo_2O_4 . The EDS and elemental mapping results confirmed the successful formation of the ternary MnCo_2O_4 phase.

The TEM, HR-TEM, elemental mapping, and EDS results of $\text{Ni}_{0.8}\text{Mn}_{0.2}\text{Co}_2\text{O}_4$ (NMCO4) are shown in Figures 3 and 4. The TEM image of the NMCO4 revealed a uniform formation of 3D nanoflower-like nanostructures on the surface of NMCO4 thin film (Figure 3A-F). In

addition, the average diameter and thickness of the individual nanoflowers were approximately 400–500 and 20–30 nm, (marked in Figure 3B), respectively. The marked area of the TEM images revealed the uniform decoration of the NMCO4 nanoflowers with a very low size of the NPs. The average size of the NPs is approximately 2 ± 4 nm, as shown in the marked Figure 3G. In addition, the transparent area of the HR-TEM image of the NMCO4 thin films revealed that the nanostructures were highly porous as shown in Figure 3G. These porous heterostructures of the NMCO4 nanostructures increased the specific surface area of the nanostructure, thus enhancing its electrochemical performance compared to those of the other samples.^{28,29} In addition, the surface of the NPs-decorated NFs provided an easy pathway, like a “superhighway,” for the ion/electron transfer, thus improving the electrochemical performance of the $\text{Ni}_{0.8}\text{Mn}_{0.2}\text{Co}_2\text{O}_4$ thin film.

Two different interplanar spacings were observed in the HR-TEM image of $\text{Ni}_{0.8}\text{Mn}_{0.2}\text{Co}_2\text{O}_4$, which corresponds to the successful formation of the hybrid phase of NiCo_2O_4 and MnCo_2O_4 (Figure 3H). These included the lattice spacing of 0.23 nm, which was associated with the plane of NiCo_2O_4 (222), and the lattice spacing of 0.29 nm (220), which was ascribed to the planes of MnCo_2O_4 . In addition, similar results were observed in the selected area electron diffraction (SAED) patterns of the $\text{Ni}_{0.8}\text{Mn}_{0.2}\text{Co}_2\text{O}_4$. Dark and black rings were observed in the SAED patterns of the $\text{Ni}_{0.8}\text{Mn}_{0.2}\text{Co}_2\text{O}_4$ thin films, which were related to the NiCo_2O_4 and MnCo_2O_4 , respectively, which strongly indicates the presence of both phases of NiCo_2O_4 and MnCo_2O_4 materials. The electrode fabricated using this hybrid hetero nanostructure provided fast ion/electron transfer, thus enhancing the charger/discharger reaction and material stability of the electrode. Figure 4A–F show the elemental mapping and EDS spectra of the NMCO4 thin film. The elemental mapping and EDS results confirmed the presence and uniform formation of Ni, Mn, Co, and O elements on the surface of $\text{Ni}_{0.8}\text{Mn}_{0.2}\text{Co}_2\text{O}_4$, which confirmed the formation of the pure quaternary $\text{Ni}_{0.8}\text{Mn}_{0.2}\text{Co}_2\text{O}_4$ phase. In addition, the atomic percentages of Ni, Mn, Co, and O were 18.33, 13.69, 26.82, and 41.16%, respectively (Figure 4F).

3.2 | Brunauer-Emmett-Teller (BET) analysis

To further investigate the porosity of the nanostructure, BET analysis was performed to obtain extensive

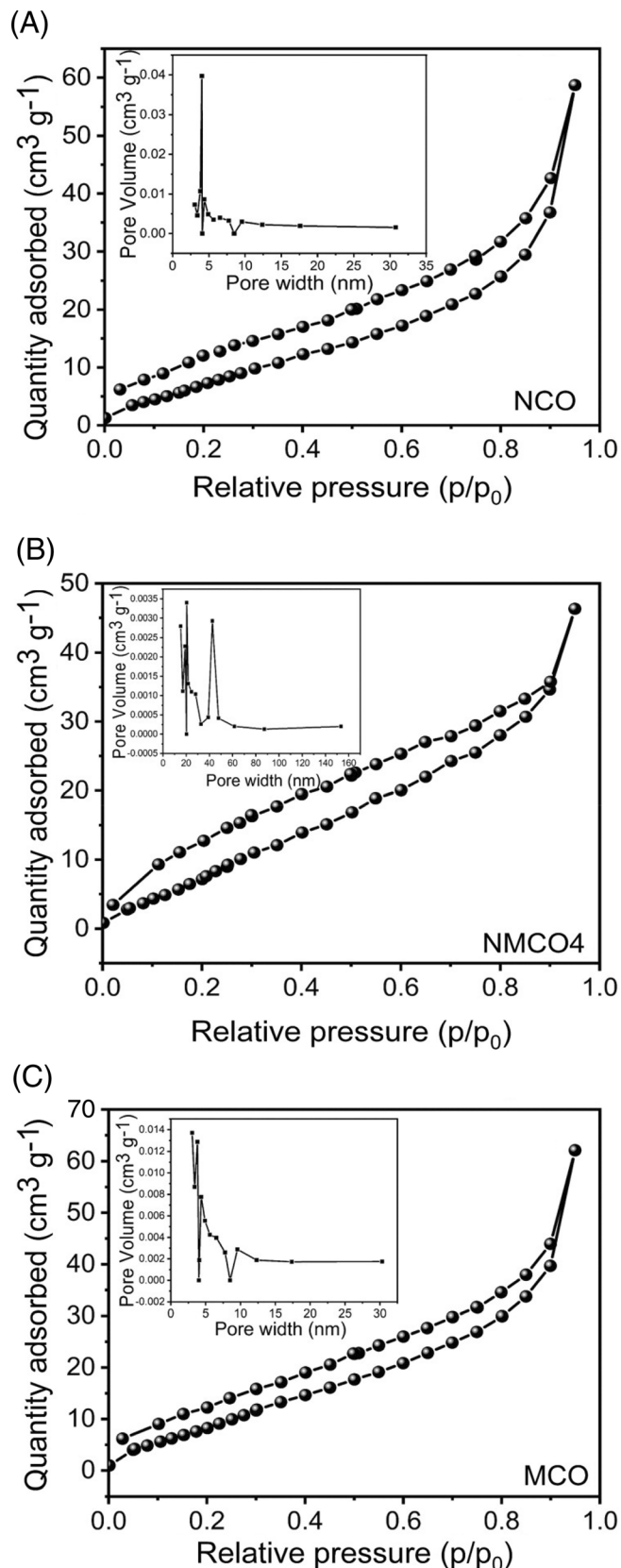


FIGURE 5 (A–C) BET and inset show the pore size distributions of the NCO, NMCO4, and MCO composite thin films

information on the specific surface area (SSA) and pore distribution of the NiCo_2O_4 , $\text{Ni}_{0.8}\text{Mn}_{0.2}\text{Co}_2\text{O}_4$, and MnCo_2O_4 thin films. Figure 5A–C shows the BET results of the NiCo_2O_4 , $\text{Ni}_{0.8}\text{Mn}_{0.2}\text{Co}_2\text{O}_4$, and MnCo_2O_4 thin films, and the insets show their pore-size distribution. The BET curves of all the samples exhibited typical IV isotherms with H3-type hysteresis loops, indicating the existence of a mesoporous-like nanostructure in the samples. This mesoporous-like nanostructure significantly increased the SSA of the samples.³⁰ In addition, the SSA of $\text{Ni}_{0.8}\text{Mn}_{0.2}\text{Co}_2\text{O}_4$ ($40.26 \text{ m}^2 \text{ g}^{-1}$) was significantly higher than those of the ternary NiCo_2O_4 ($32.49 \text{ m}^2 \text{ g}^{-1}$) and MnCo_2O_4 ($25.29 \text{ m}^2 \text{ g}^{-1}$) thin films. Furthermore, among the samples, $\text{Ni}_{0.8}\text{Mn}_{0.2}\text{Co}_2\text{O}_4$ exhibited the best electrochemical performance, which could be attributed to the decoration of the nanoparticle on the highly-flexible nanoflakes.³¹

The pore-size distribution of samples was calculated using the Barrett-Joyner-Halenda (BJH) method, and the results are shown in the inset of Figure 5A–C, respectively. The calculated pore sizes of the NiCo_2O_4 , $\text{Ni}_{0.8}\text{Mn}_{0.2}\text{Co}_2\text{O}_4$, and MnCo_2O_4 thin films were 2.16, 1.92, and 2.10 nm, respectively.³² These values indicate that the samples were composed of a highly mesoporous-like nanostructure, which enhanced the electrochemical performance and electron/ion transfer of the $\text{Ni}_{0.8}\text{Mn}_{0.2}\text{Co}_2\text{O}_4$. We believe that this is the main reason for the enhancement in the supercapacitor performance and electrocatalytic activity of the $\text{Ni}_{0.8}\text{Mn}_{0.2}\text{Co}_2\text{O}_4$ electrodes compared to those of the other electrodes.³³

3.3 | Structural studies

The structure and phase of the as-prepared NCO, NMCO4, NMCO3, NMCO2, NMCO1, and MCO thin films were examined using XRD, and the results are shown in Figure 6A. The XRD patterns of all the samples exhibited a polycrystalline nature with mixed phases of NiCo_2O_4 and MnCo_2O_4 . Seven minor peaks were observed in the XRD pattern of NCO at $2\theta = 32.66, 36.62, 39.00, 45.10, 54.58, \text{ and } 58.31^\circ$, which corresponded to the (220), (311), (222), (400), (422), and (511) planes, respectively, indicating the polycrystalline nature of the cubic crystal structure. These peaks are consistent with the standard JCPD cards (00-020-0781) of the cubic crystal structure of the pure phase of ternary NiCo_2O_4 .³⁴ The XRD patterns of the Ni and Mn composite and its version are shown in NMCO4 to NMCO1 thin films (Figure 6A). The XRD patterns of the NMCO4 to NMCO1 thin films were similar to those of the ternary NCO and MCO thin films. However, the XRD patterns of the NMCO4 thin film were significantly different from those of the NMCO1, NMCO2, and NMCO3

composite. Peaks were observed in the XRD pattern of NMCO4 at $2\theta = 24.51, 32.66, 36.62, 39.00, 45.10, 54.58, \text{ and } 58.31^\circ$, which corresponded to the (001), (220), (311), (222), (400), (422) and (511) planes, respectively, indicating the formation of the NiCo_2O_4 and MnCo_2O_4 compounds. In addition, the peaks at $32.66, 36.62, 39.00, 45.10, 54.58, \text{ and } 58.31^\circ$, which were ascribed to (220), (311), (222), (400), (422), and (511) planes, suggested the formation of the ternary phase of the MnCo_2O_4 compound. The XRD patterns of the NMCO4, NMCO3, NMCO2, and NMCO1 thin films indicate the presence of a double-layered heterostructure with the formation of the mixed phases of the ternary $\text{Ni}_{1-x}\text{Mn}_x\text{Co}_2\text{O}_4$.^{30,35–37} Six peaks were observed in the XRD patterns of the MCO at $2\theta = 32.66, 36.62, 39.00, 45.10, 54.58, \text{ and } 58.31^\circ$, which corresponded to the (220), (311), (222), (400), (422), and (511) planes of MnCo_2O_4 (JCPDS file no. 00-023-1237), respectively.^{36,37} The XRD patterns of the NCO, MCO, and $\text{Ni}_{1-x}\text{Mn}_x\text{Co}_2\text{O}_4$ ($X = 0.2, 0.4, 0.6, 0.8$) heteronanostructure thin films confirm the presence of the pure phase of NiCo_2O_4 , MnCo_2O_4 , and a mixed phase of $\text{NiCo}_2\text{O}_4/\text{MnCo}_2\text{O}_4$ heterophase, which indicates the formation of the pure ternary and quaternary double-layered heterostructures of NiCo_2O_4 , MnCo_2O_4 , and a mixed phase of $\text{NiCo}_2\text{O}_4/\text{MnCo}_2\text{O}_4$ compound. These results indicate that the DES method is suitable for the preparation of various ternary and quaternary compounds.

The chemical compositions of the as-prepared NiCo_2O_4 , MnCo_2O_4 , and $\text{Ni}_{0.8}\text{Mn}_{0.2}\text{Co}_2\text{O}_4$ hybrid nanostructure were further investigated using XPS analysis, and the results are shown in Figures S4 and S5, and Figure 6B–E. Figure S4 shows the survey scan XPS results of the NiCo_2O_4 , MnCo_2O_4 , and $\text{Ni}_{0.8}\text{Mn}_{0.2}\text{Co}_2\text{O}_4$ thin films. The XPS survey scan confirms the presence of Ni, Co, O elements in the NiCo_2O_4 ; Mn, Co, O elements in the MnCo_2O_4 ; and Ni, Mn, Co, and O elements in the $\text{Ni}_{0.8}\text{Mn}_{0.2}\text{Co}_2\text{O}_4$ compound, which indicates the formation of the ternary NiCo_2O_4 and MnCo_2O_4 and mixed-phase $\text{Ni}_{0.8}\text{Mn}_{0.2}\text{Co}_2\text{O}_4$ compounds. Figure 6B–E and Figure S5A–F show the Ni 2p, Mn 2p, Co 2p, and O 1s core-level spectra of the $\text{Ni}_{0.8}\text{Mn}_{0.2}\text{Co}_2\text{O}_4$, NiCo_2O_4 , and MnCo_2O_4 thin films, respectively. Four main peaks were observed in the Ni 2p core-level spectrum. Two of these two spin-orbits were the Ni 2p doublets, whereas the remaining two peaks were related to the satellite peaks of Ni 2p (Figure 6B and Figure S5a). The first two major peaks were observed at 873.16 and 855.60 eV, which corresponded to Ni 2p_{1/2} and Ni 2p_{3/2}, respectively. The difference between the Ni 2p doublets was approximately 17.56 eV, which indicates the presence of the Ni^{2+} species in the NMCO4 samples.³⁸ The remaining two peaks were observed at 880.61 and 863.60 eV and corresponded to the satellite of Ni^{2+} species. Figure 6C shows the Mn 2p core-level spectrum of the NMCO4 compound. Two

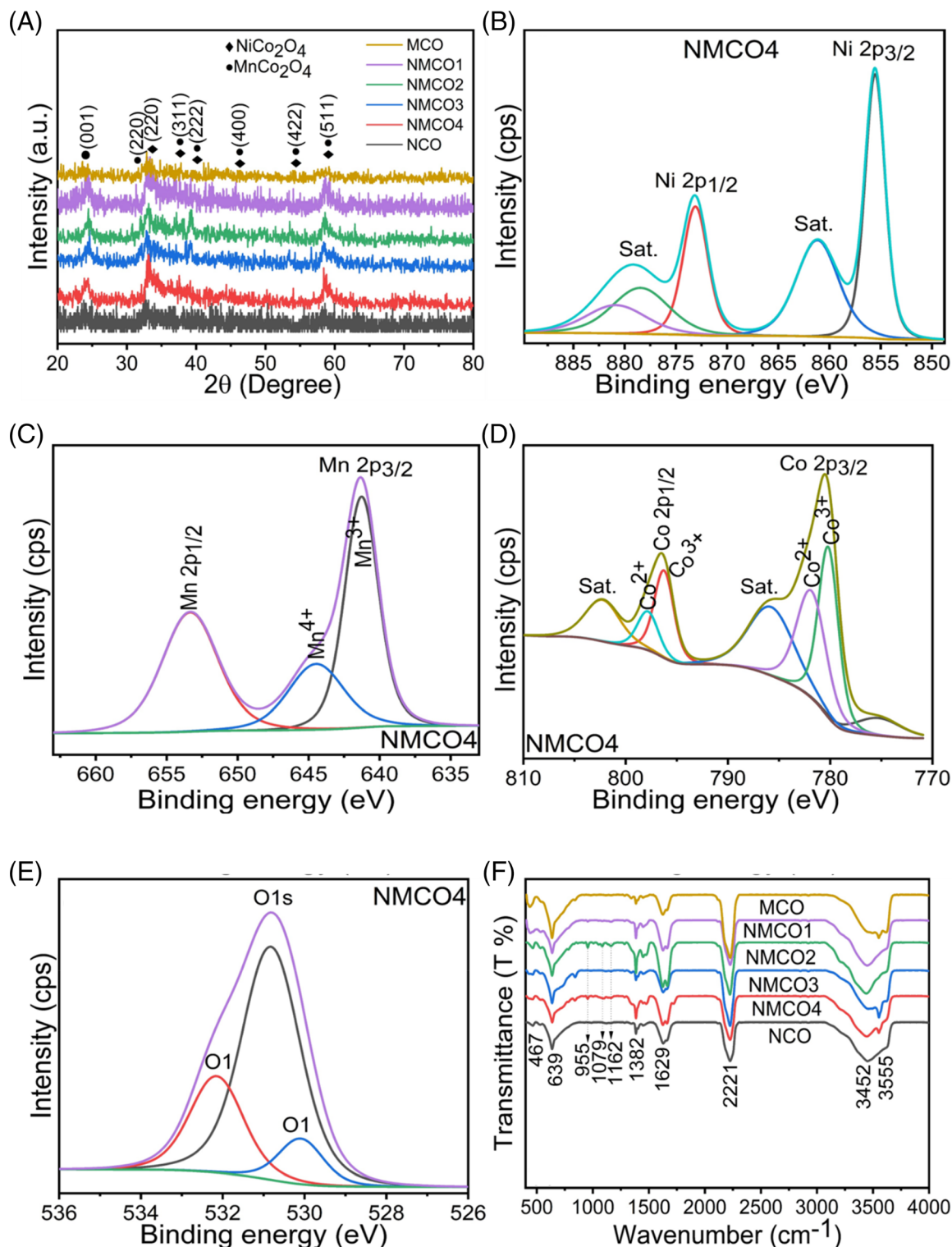


FIGURE 6 (A) XRD patterns of NCO, NMCO4, NMCO3, NMCO2, NMCO1, and MCO composites, (B) High resolution of Ni 2p, (C) high resolution of Mn 2p, (D) high resolution of Co 2p, and (E) high resolution of O 1 s, spectra of the optimized NMCO4, respectively. (F) FT-IR spectra for the NCO, NMCO4, NMCO3, NMCO2, NMCO1, and MCO composites

spin-orbit doublet peaks were observed at binding energies of 653.16 and 641.36 eV, which could be ascribed to Mn 2p_{1/2} and Mn 2p_{3/2}, respectively. The difference in

the binding energy between the two levels of Mn 2p_{1/2} and Mn 2p_{3/2} was approximately 11.80 eV, which corresponded to the presence of Mn³⁺; however, an additional

peak was observed at 644.26 eV, which corresponded to the presence of Mn^{4+} species. This indicates the presence of Mn^{4+} states in the sample.¹³ The Co 2p core-level spectrum is shown in Figure 6D and Figure S5b, e). Six peaks were observed in the Co 2p core-level spectrum. Out of these peaks, two major peaks were observed at 796.46 and 780.54 eV, which corresponded to the spin–orbit species of Co 2p_{1/2} and Co 2p_{3/2}, respectively. Additional peaks were observed at binding energies of 796.24 and 780.19 eV, which corresponded to the presence of the Co^{3+} . The two peaks observed at binding energies of 797.91 and 782.06 eV, which were attributed to Co 2p_{1/2} and Co 2p_{3/2}, respectively, indicated the existence of Co^{2+} species. These four main peaks suggest that Co^{2+} and Co^{3+} species were present in the as-prepared $\text{Ni}_{0.8}\text{Mn}_{0.2}\text{Co}_2\text{O}_4$ thin film. The remaining two peaks observed at the binding energies of 802.33 and 885.96 eV were related to the shakeup satellite peaks of Co^{2+} .^{13,33} Three main peaks were observed in the O 1s core-level spectrum at binding energies of 532.16, 530.79, and 530.09 eV, which corresponded to the presence of metal hydroxide (M–OH), metal–oxygen, and oxygen bonds, respectively, in the sample (Figure 6E, Figure S5c,f). XPS analysis confirmed the formation of pure ternary NiCo_2O_4 , MnCo_2O_4 , and quaternary $\text{Ni}_{0.8}\text{Mn}_{0.2}\text{Co}_2\text{O}_4$ compounds.

3.4 | Fourier transform infrared spectroscopic studies

The functional and vibration groups of the NCO, NMCO4 to NMCO1, and MCO thin films were examined using FT-IR spectroscopy, and the results are shown in Figure 6F. The main absorption peaks in the FT-IR spectra of the films were observed at 467 and 639 cm^{-1} , which could be attributed to the vibrational bending modes of Ni–O/Co–O, and Mn–O compounds, respectively.^{13,33} The absorption peaks corresponding to the stretching vibration mode of Ni–O and Co–O were overlapped at 467 cm^{-1} . Additional absorption peaks were observed at 1162 and 1382 cm^{-1} , which corresponded to the C–C and C–O–C vibration stretching modes.³⁹ Furthermore, two additional vibration bands were observed at 955 and 1079 cm^{-1} , which corresponded to the characteristic mode of C–N vibration bonds. In addition, three characteristic peaks were observed at 1629, 3452, and 3555 cm^{-1} , which corresponded to the –OH stretching vibration mode, which could be attributed to the fact that all the samples were prepared in double-distilled water.¹³ The FT-IR analysis results of this study are consistent with those of previous studies.^{40,41}

3.5 | Electrochemical performance of the $\text{Ni}_{1-x}\text{Mn}_x\text{Co}_2\text{O}_4$ films

The electrochemical performance of the hierarchical hybrid nanostructured NCO, NMCO4, NMCO3, NMCO2, NMCO1, and MCO electrodes were investigated using CV and GCD in a three-electrode system with an Ag/AgCl reference electrode and 1 M KOH aqueous electrolyte. Figure 7A–C and Figure S6a–c show the typical CV curves of all the $\text{Ni}_{1-x}\text{Mn}_x\text{Co}_2\text{O}_4$ electrodes (NCO, NMCO4, NMCO3, NMCO2, NMCO1, and MCO) at different scan rates in the range from 2 to 20 mV s^{-1} . The CV curves of all the electrodes exhibited a strong pair of redox and oxidation current peaks, which could be attributed to the reversible Faradaic reaction process due to the electrochemical behavior of $\text{Ni}^{2+}/\text{Ni}^{3+}/\text{Co}^{2+}/\text{Co}^{3+}$ and $\text{Mn}^{3+}/\text{Mn}^{4+}$, respectively.³¹ The comparison of the CV curves of all the samples revealed that NMCO4 had the largest area under the CV curve, indicating that $\text{Mn}^{3+}/\text{Mn}^{4+}$ and $\text{Ni}^{2+}/\text{Ni}^{3+}$ ions play an important role in enhancing the electrochemical activity of NiCo_2O_4 and MnCo_2O_4 , respectively. This suggests that the positive synergistic effect between Ni–Mn–Co ions increased the Cs of the prepared electrodes.³² A fine observation, the CV curves of the electrodes exhibited different shapes with a change in the values of Ni and Mn ($X = 0, 0.2, 0.4, 0.6, 0.8$, and 1), which could be attributed to the different redox reactions between Ni–Co, Ni–Mn–Co, and Mn–Co ions and the co-existence of OH^- .

Figure 7A–C shows the CV curves of the NiCo_2O_4 , $\text{Ni}_{0.8}\text{Mn}_{0.2}\text{Co}_2\text{O}_4$, and MnCo_2O_4 electrodes at various scan rates from 2 to 20 mV s^{-1} , within a potential window of 0 to 0.5, and –0.2 to 0.6 V, respectively, and the CV curves of NMCO3, NMCO2, and NMCO1 are shown in supporting information Figure S6a–c, respectively. The oxidation peak of the CV curves of the electrodes shifted towards a higher negative potential and the reduction peaks shifted towards a higher potential with an increase in the scan rate. In addition, the comparison of the CV curves of the electrodes revealed that the current density of the NMCO4 electrode (443 mA cm^{-2}) was larger than those of the NCO (157 mA cm^{-2}), NMCO3 (330 mA cm^{-2}), NMCO2 (276 mA cm^{-2}), NMCO1 (230 mA cm^{-2}), and MCO (330 mA cm^{-2}) electrodes, indicating its superior supercapacitor performance. Figure 7D shows the Cs of the NCO, NMCO4 to NMCO1, and MCO electrodes at different scan rates, respectively. At lower scan rates (2 mV s^{-1}), the Cs of the NCO, NMCO4, NMCO3, NMCO2, NMCO1, and MCO electrodes were 267, 699, 351, 525, 338, and 206 mAh g^{-1} , respectively. The high Cs of the NMCO4 electrode (699 mAh g^{-1}) could be attributed to the small size of the spherical NPs uniformly coated on the porous,

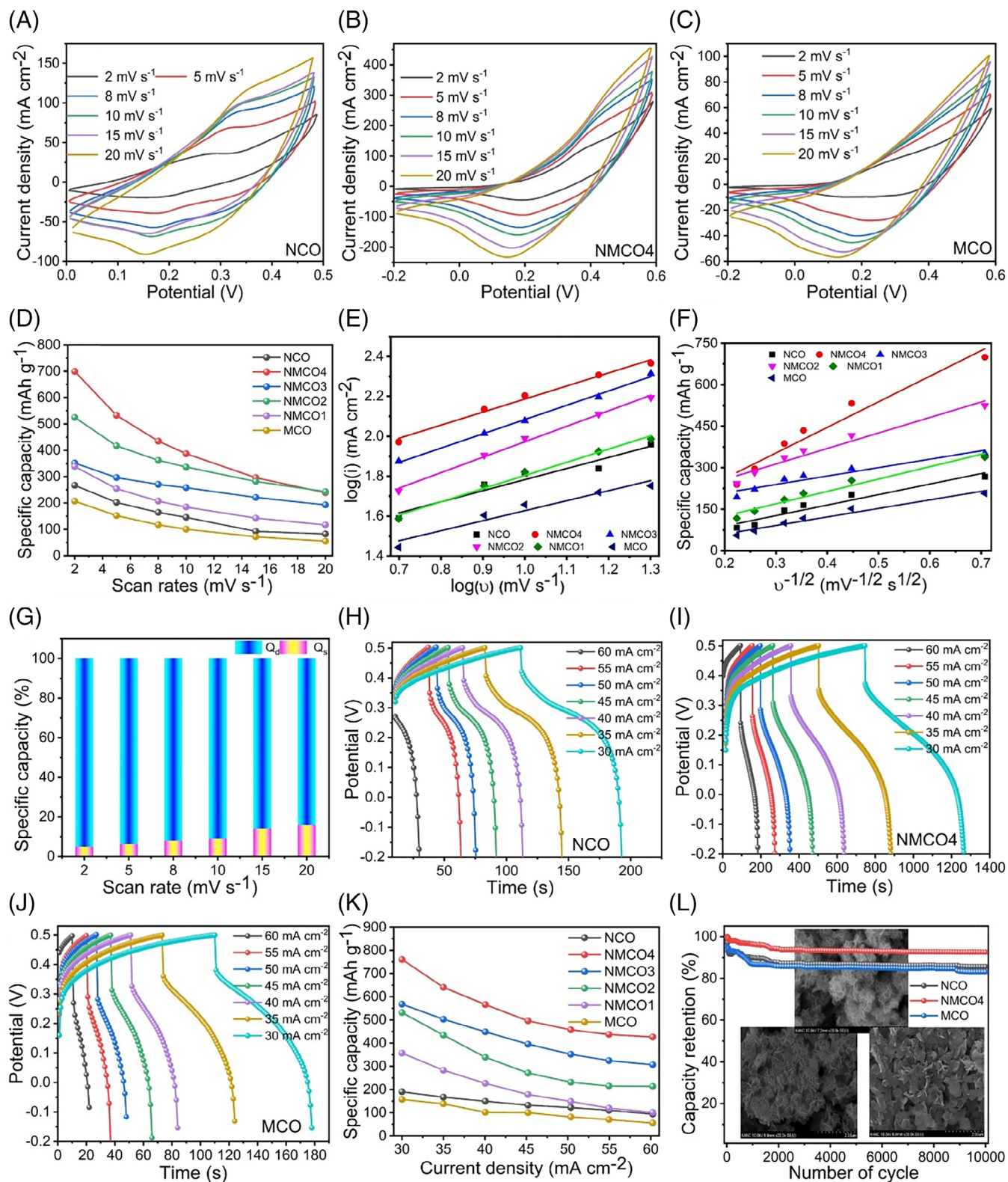


FIGURE 7 (A-C) CV measurements of NCO, NMCO4, and MCO electrodes, at different scan rates 2–20 mV s^{-1} , respectively, (D) specific capacity of NCO, NMCO4, NMCO3, NMCO2, NMCO1, and MCO electrodes at a different scan rate, (E) $\log(i)$ vs $\log(v)$ of NCO, NMCO4, NMCO3, NMCO2, NMCO1, and MCO electrodes, (F) specific capacity with the square root of the scan rate, (G) Q_d vs Q_s of the NMCO4 electrodes, (H–J) GCD curves of NCO, NMCO4, and MCO electrodes at different current densities in the range 30–60 mA cm^{-2} , (K) specific capacity of NCO, NMCO4, NMCO3, NMCO2, NMCO1, and MCO electrodes with different current densities, (i) Cycling stability of the synthesized NCO, final optimized NMCO4, and MCO electrodes at constant scan rates 100 mV s^{-1} up to 10 000 cycles, inset shows the FE-SEM images of after cycling stability

interconnected vertically-grown NFs-like nanostructures. The hybrid surface morphology of NMCO4 increased its SSA and significantly enhanced its ion/electron transfer.^{28–31} Kandula et al.²⁸ synthesized metal sulfide materials with different ratios of the M (M = Ni, Co, Zn) ions for effective application in supercapacitors. They prepared the composite between the layered double NiCo(OH)₂ and metal sulfide with the different ratios of the M. They found 1D nanowire, NPs, and nanoflakes like surface morphology of the prepared materials. Also, they mentioned the values of the Cs of the optimized electrode of 404 mAh g^{−1} at a current density of 3 mA cm^{−2} with better stability up to 93.2% for 10 000 cycles.³⁰ Wang et al.³² reported the nanosheets like ultrathin NiCO-MOF electrode material for the supercapacitors by ultrasonication method. They mentioned the high Cs of the NiCO-MOF electrode is 1202.1 F g^{−1} at a current density of 1 A g^{−1}, respectively. Because they mentioned that the ultrathin-like nanosheets of NiCO-MOF electrodes provided a faster path and more surface area for improving the supercapacitor properties. The available reports in a previous study and comparative Table S1 indicate the Ni_{0.8}Mn_{0.2}Co₂O₄ electrode is a better option for electrochemical applications than the ternary NiCo₂O₄ and MnCo₂O₄ electrode materials.

A pair of redox peaks are observed for all the samples along with an increase in area under the curve at different scan rates indicating superior rate capability and improved mass transport. The charge hybridization kinetics is a clear understanding based on the current response at scan rate. The fundamental relation is as follows,^{41,42}

$$i = av^b$$

In which 'a' and 'b' are the adjustable parameters. The b value links to the charging kinetics which is equal to the slope of log (i) vs log v (Figure 7E). The charge stored includes capacitive controlled (Q_s) redox reaction and diffusion controlled (Q_d) redox process indicating when 'b' values are 1 and 0.5 respectively.^{41,42} The 'b' value of the samples namely NCO, NMCO1, NMCO2, NMCO3, NMCO4, and MCO is 0.55, 0.65, 0.71, 0.77, 0.66, and 0.50, respectively implying both capacitive and diffusion-controlled battery type nature.⁴²

Further, the charge contribution is estimated by using the following equation and corresponding results.

$$Q_t = Q_s + kv^{1/2}$$

where k is constant and v is the scan rate. The Q_s can be evaluated by assuming v goes tend to infinity from the plot Q_t vs v^{−1/2} (Figure 7F). The percentage charge

contribution of the samples at different scan rates is depicted in Figure 7A and Figure S7a–e. It reveals that the diffusion contribution increases with lowering the scan rate owing to the large time consumption for the diffusion of ions into the lattices.⁴³

The electrochemical behavior of the prepared electrodes was further investigated using charge-discharge measurements, and the results are shown in Figure 7H–J and supporting information in Figure S6d–f. Among the electrodes, the NMCO4 exhibited the highest charge-discharge time (1280 s), which significantly enhanced its C_{sp} (761 mAh g^{−1}) at a lower current density (30 mA cm^{−2}). The electrochemical performance of composite electrodes improved systemically with an increase in the percentage of Ni and Mn (X values). At current densities of 30, 35, 40, 50, 55, and 60 mA cm^{−2}, the Cs values of the NMCO4 electrode was 761, 640, 566, 495, 457, 437, and 426 mAh g^{−1}, respectively. The Cs values of NMCO4 at a current density of 30 mA cm^{−2} were 3.6 and 4.2 times higher than those of the pure NiCo₂O₄ (190 mAh g^{−1}), and MnCo₂O₄ (157 mAh g^{−1}) samples, respectively (Figure 7K). At all current densities in the range from 30 to 60 mA cm^{−2}, the Cs of Ni_{0.8}Mn_{0.2}Co₂O₄ (NMCO4) were higher than those of the other electrodes, which is consistent with the CV and Cs calculated from the CV curve. The highest Cs (761 mAh g^{−1}) was achieved at a current density of 30 mA cm^{−2}, and the Cs at a high current density of 60 mA cm^{−2} was 426 mAh g^{−1}. The Cs values achieved in this study are higher than those of previously reported supercapacitor electrodes, such as MnCo₂O₄@Ni(OH)₂ belt-based core-shell nanoflowers (300 mAh g^{−1} at 5 A g^{−1}),⁴⁴ NiCo₂O₄@Co-Fe LDH core-shell nanowire arrays (216 mAh g^{−1} at 1 A g^{−1}),⁴⁵ hierarchical MnCo₂O₄-NiCo₂O₄ (192 mAh g^{−1} at 1 A g^{−1}),⁴⁶ flowers MnCo₂O₄ hollow nanosphere (72 mAh g^{−1} at 1 A g^{−1}),⁴⁷ N doped carbon nanofibers coated MnCo₂O₄ NPs (120 mAh g^{−1} at 0.5 A g^{−1})⁴⁸ and Fe/Ni(LDH)-CN-Fe/Ni-PBAs (187 mAh g^{−1} at 1 A g^{−1}).⁴⁹

The cycling stability of electrodes is one of the parameters used to examine their practical application for device fabrication. The cycling life of the NCO, NMCO4, and MCO electrodes was investigated using CV measurements at 20 mV s^{−1} for 10 000 cycles, and the results are shown in Figure 7I. The NCO, NMCO4, and MCO electrodes exhibited cycling retention of 85.80, 92.86, and 83.06%, respectively, after the last cycles. After the cycling study, surface morphology results show the NMCO4 electrode is quite stable after the last cycles (as shown in the inset of Figure 7I). The Ni_{0.8}Mn_{0.2}Co₂O₄ electrode was more stable than the NiCo₂O₄, and MnCo₂O₄ electrodes.⁵⁰ The enhanced retention capacity stability of the Ni_{0.8}Mn_{0.2}Co₂O₄ electrode could be attributed to the fact that the hybrid nanostructures-like NPs decorated on the

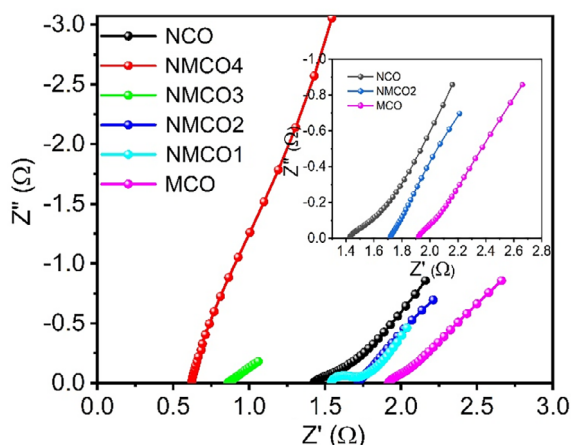


FIGURE 8 Nyquist plots of NCO, NMCO4, NMCO3, NMCO2, NMCO1, and MCO composite electrodes

highly porous nanoflakes enhanced the surface area of $\text{Ni}_{0.8}\text{Mn}_{0.2}\text{Co}_2\text{O}_4$, and could also be attributed to the strong bonding between the NPs and nanoflakes.⁵¹

To further understand the kinetic mechanisms of the electrodes, their electrochemical performance was examined using EIS analysis. Figure 8 shows the Nyquist plots of the NCO, NMCO4-NMCO1, and MCO electrodes, and the insets show their zoom plots. The low-frequency region indicates the supercapacitor-like behavior of the prepared electrodes. The Nyquist plot of NMCO4 exhibited an exactly vertical straight line compared to those of the NCO, NMCO3, NMCO2, NMCO1, and MCO electrodes, which indicates the higher electrical conductivity and low resistance of the NMCO4 electrode. The solution resistance (R_s) and charge transfer resistance (R_{ct}) were calculated using the standard equivalent circuit (as shown in the inset of Figure 9I). The R_s value of the NMCO4 electrode (0.53 Ω) was lower than those of NCO (1.40 Ω), NMCO3 (1.7 Ω), NMCO2 (0.79 Ω), NMCO1 (1.55 Ω), and MCO (1.9 Ω). The R_{ct} values of the NCO, NMCO4, NMCO3, NMCO2, NMCO1, and MCO electrodes were 0.51, 0.014, 0.11, 0.13, 0.32, and 0.16 Ω , respectively. The NMCO4 electrode exhibited lower R_s and R_{ct} values than the other electrodes, which indicates that NMCO4 provided a faster charge transfer rate, as well as Faradaic redox reactions. Consequently, this improved the electrochemical performance of the NMCO4 electrode. The EIS analysis results indicated that NMCO4 exhibited higher electrical conductivity than the other electrodes.^{23,50,51}

3.6 | Asymmetric Solid-State hybrid SC (HSC) device

To investigate the practical application of the optimized $\text{Ni}_{0.8}\text{Mn}_{0.2}\text{Co}_2\text{O}_4$ electrode, we constructed a two-electrode

solid-state asymmetric HSC cell using the optimized quaternary $\text{Ni}_{0.8}\text{Mn}_{0.2}\text{Co}_2\text{O}_4$ electrode as the positive electrode, AC powder used as the negative electrode, and KOH/PVA coated printing paper as the separator. Figure 9A shows the CV measurements of the $\text{Ni}_{0.8}\text{Mn}_{0.2}\text{Co}_2\text{O}_4//\text{AC}$ with different potential windows at a constant scan rate of 100 mV s^{-1} . As shown in Figure 9A, the active potential window of the asymmetric device is fixed between 0.0 and 1.6 V. Figure 9B shows the CV curves of the solid-state asymmetric $\text{Ni}_{0.8}\text{Mn}_{0.2}\text{Co}_2\text{O}_4//\text{AC}$ at different scan rates from 5 to 100 mV s^{-1} . The CV curves exhibited similar positive and negative current densities, which could be attributed to the occurrence of the Faradaic reactions.^{23,41,44} In addition, with an increase in the scan rate from 5 to 100 mV s^{-1} , the current density increased and the CV curve became more rectangular, indicating the long-term stability and improved electrochemical properties of the $\text{Ni}_{0.8}\text{Mn}_{0.2}\text{Co}_2\text{O}_4//\text{AC}$ device.⁴⁵⁻⁴⁷ The GCD curves of the device at a constant current density with an increase in the potential window from 0 to 1.6 V are shown in Figure 9C. Figure 9D shows the GCD curves of the solid-state asymmetric HSC $\text{Ni}_{0.8}\text{Mn}_{0.2}\text{Co}_2\text{O}_4//\text{AC}$ device at different current densities from 15 to 30 mA cm^{-2} . At lower current densities, the discharging time shows very low Ir values ($\text{Ir} = 0.0\text{--}0.1$ V), which indicates that the asymmetric HSC exhibited higher cycling stability rates and rate retention capacity. Figure 9E shows the Cs values calculated from the GCD curves at various current densities from 15–30 mA cm^{-2} . The calculated Cs value of the solid-state asymmetric HSC $\text{Ni}_{0.8}\text{Mn}_{0.2}\text{Co}_2\text{O}_4//\text{AC}$ device at a current density of 15 mA cm^{-2} was 298 mAh g^{-1} . The coulombic efficiency of the present fabricated solid-state asymmetric HSC $\text{Ni}_{0.8}\text{Mn}_{0.2}\text{Co}_2\text{O}_4//\text{AC}$ device provided better electrical properties (Figure 9F).

The long-term durability and retraction capacity are important parameters for the practical application of solid-state HSC in electric devices and electric motors.⁵¹ Figure 9G shows the cycling stability of the solid-state asymmetric HSC $\text{Ni}_{0.8}\text{Mn}_{0.2}\text{Co}_2\text{O}_4//\text{AC}$ device based on GCD curves for 5000 cycles at a constant current density of 27 mA cm^{-1} . The $\text{Ni}_{0.8}\text{Mn}_{0.2}\text{Co}_2\text{O}_4//\text{AC}$ device exhibited a good retention capacity up to 92.69% after 5000 GCD cycles. The inset in Figure 9G shows the first and some selected GCD cycles at the same potential window and current density. The image in Figure 9G indicates that the quaternary $\text{Ni}_{0.8}\text{Mn}_{0.2}\text{Co}_2\text{O}_4//\text{AC}$ device exhibits outstanding long-term cycling stability, suggesting the promising electrochemical application of the $\text{Ni}_{0.8}\text{Mn}_{0.2}\text{Co}_2\text{O}_4$ electrode as a positive electrode. The energy density (ED) and power density (PD) are important parameters of two-electrode devices and were calculated using standard relations 7 and 8. Figure 9H shows the Ragone plots of the solid-state asymmetric SC

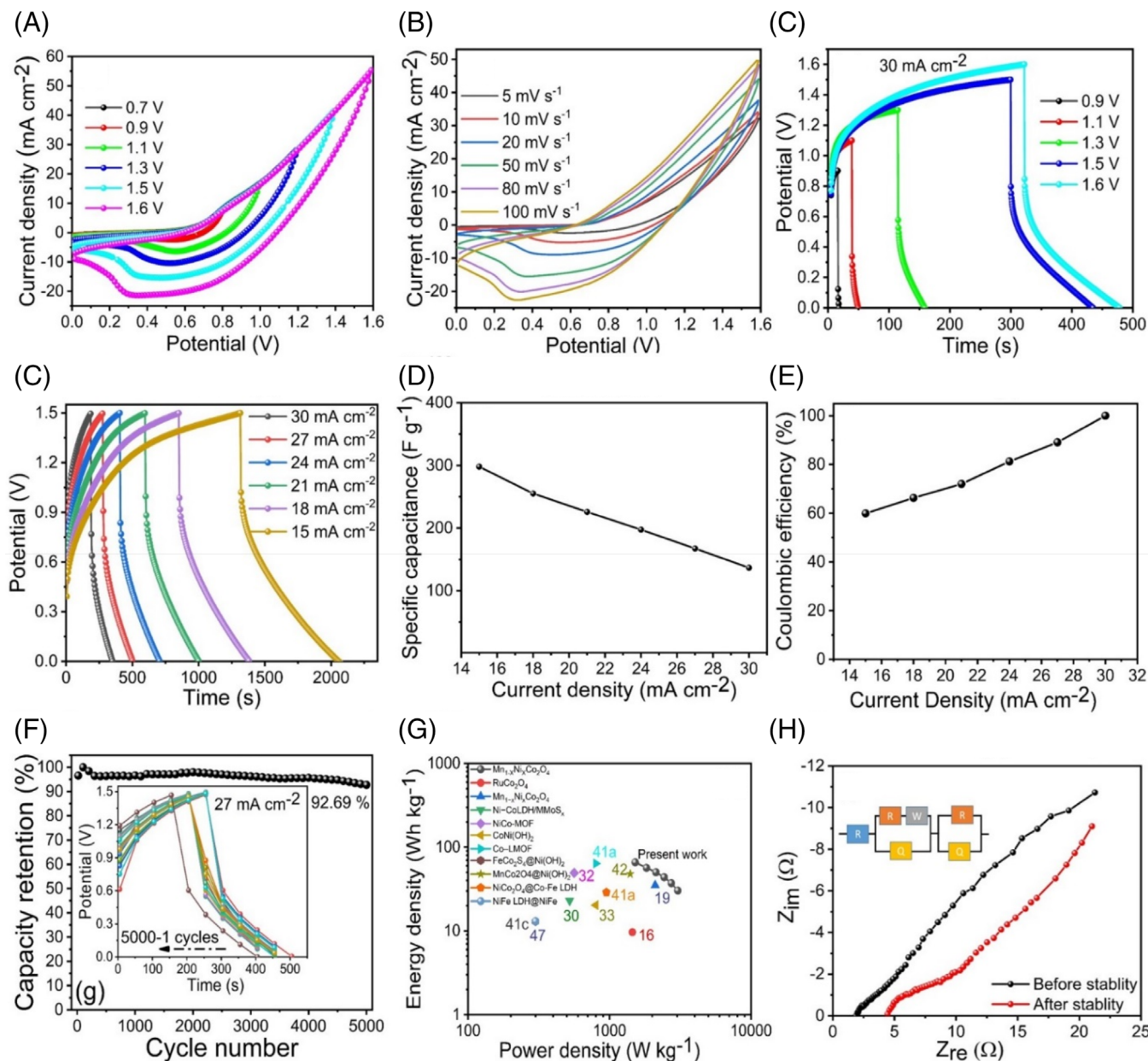


FIGURE 9 (A) Optimization of the potential window of solid-state hybrid $\text{Ni}_{0.8}\text{Mn}_{0.2}\text{Co}_2\text{O}_4/\text{AC}$ device at a constant scan rate 100 mV s^{-1} for various potential windows (0.7–1.6 V), (B) CV curves of $\text{Ni}_{0.8}\text{Mn}_{0.2}\text{Co}_2\text{O}_4/\text{AC}$ device at a constant potential window 1.6 V with different scan rates, (C) optimization of the potential window of solid-state hybrid $\text{Ni}_{0.8}\text{Mn}_{0.2}\text{Co}_2\text{O}_4/\text{AC}$ device at a constant current density 30 mA cm^{-2} for various potential window (0.9–1.6 V), (D) GCD curves of solid-state hybrid $\text{Ni}_{0.8}\text{Mn}_{0.2}\text{Co}_2\text{O}_4/\text{AC}$ device at current densities, (E, F) specific capacitance and coulombic efficiency with respect to various current densities of solid-state hybrid $\text{Ni}_{0.8}\text{Mn}_{0.2}\text{Co}_2\text{O}_4/\text{AC}$, (G) cycling retention capacity, (H) Ragone plots, (I) Nyquist plots of HSC after and before cycling stability of the hybrid $\text{Ni}_{0.8}\text{Mn}_{0.2}\text{Co}_2\text{O}_4/\text{AC}$ device

$\text{Ni}_{0.8}\text{Mn}_{0.2}\text{Co}_2\text{O}_4/\text{AC}$ based on its ED and PD. The highest obtained ED of the solid-state asymmetric HSC $\text{Ni}_{0.8}\text{Mn}_{0.2}\text{Co}_2\text{O}_4/\text{AC}$ device was 66.2 Wh kg^{-1} at a PD value of 1519 W kg^{-1} . These calculated values were higher than those of previously reported ASC devices of quaternary $\text{Ni}_{0.8}\text{Mn}_{0.2}\text{Co}_2\text{O}_4$ compounds, which indicates that this quaternary compound exhibited improved electrochemical performance, suggesting its superiority to

other ternary and binary electrodes (Table S1). The outstanding electrochemical properties of the solid-state asymmetric HSC $\text{Ni}_{0.8}\text{Mn}_{0.2}\text{Co}_2\text{O}_4/\text{AC}$ device could be attributed to its higher electrical conductivity due to its lower R_s and R_{ct} values. Figure 9I shows the Nyquist plots of the solid-state asymmetric HSC $\text{Ni}_{0.8}\text{Mn}_{0.2}\text{Co}_2\text{O}_4/\text{AC}$ device after and before cycling stability. As expected, the obtained R_s and R_{ct} values after and before

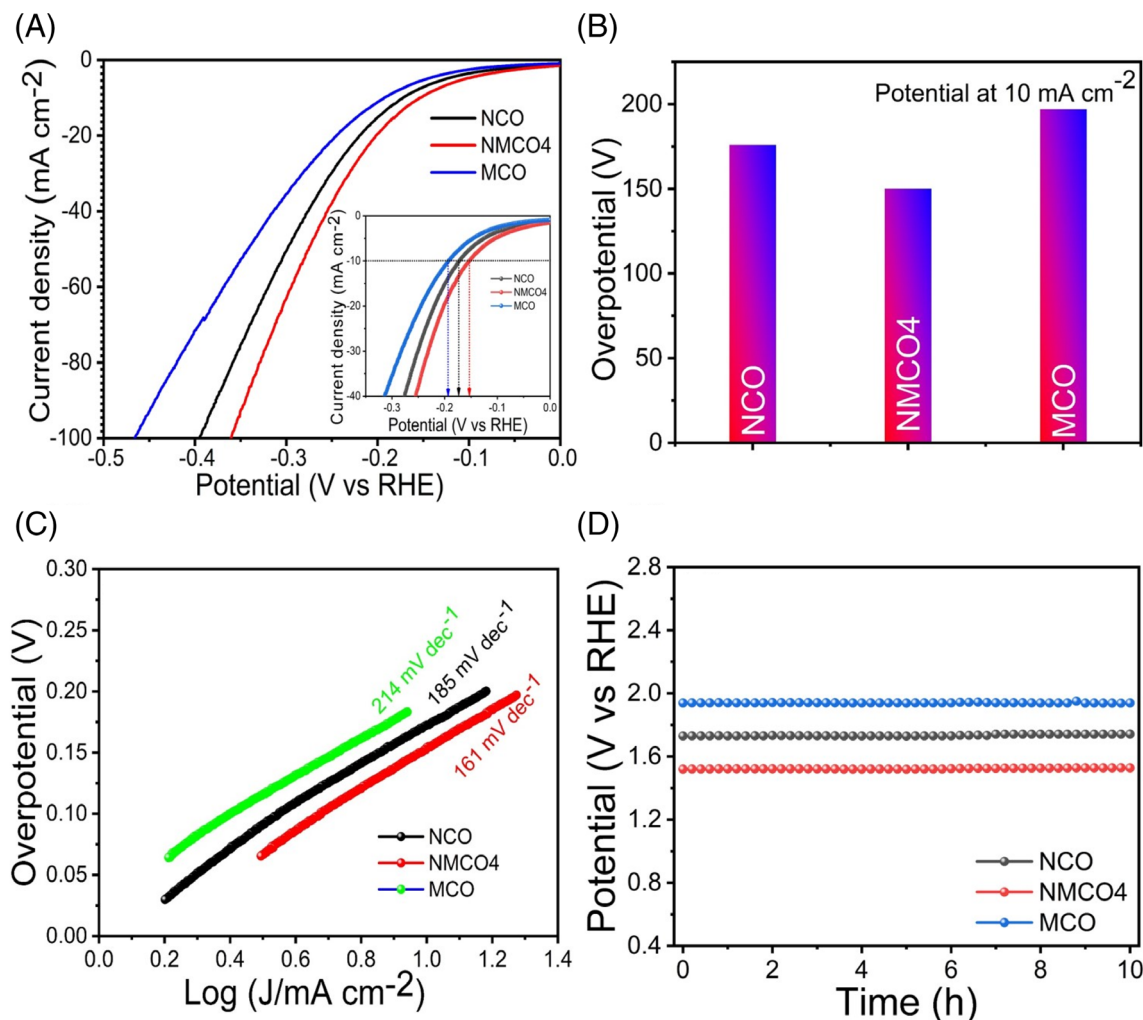


FIGURE 10 (A) HER electrochemical properties of NCO, NMCO4, and MCO electrodes in a 1 M KOH electrolyte, (B) Overpotential of the NCO, NMCO4, and MCO electrodes at constant current density 10 mA cm⁻², (C) Tafel slope of the NCO, NMCO4, and MCO electrodes, (D) Chronopotentiometric curves of NCO, NMCO4, and MCO electrodes for 10 h

the cycling stability test were similar. The R_s and R_{ct} values of the $\text{Ni}_{0.8}\text{Mn}_{0.2}\text{Co}_2\text{O}_4/\text{AC}$ device before and after the cycling stability test were 1.87 and 4.33 Ω and 2.12 and 3.15 Ω , respectively. These R_s and R_{ct} values indicate that the difference between the first and last cycle was very small, suggesting that the $\text{Ni}_{0.8}\text{Mn}_{0.2}\text{Co}_2\text{O}_4/\text{AC}$ device enhanced the active surface area of $\text{Ni}_{0.8}\text{Mn}_{0.2}\text{Co}_2\text{O}_4$ and provided a faster ion/electron pathway.²³

3.7 | HER and OER studies

To prove the multiple application of the as-prepared NiCo_2O_4 (NCO), $\text{Ni}_{0.8}\text{Mn}_{0.2}\text{Co}_2\text{O}_4$ (NMCO4), and MnCo_2O_4 (MCO) electrodes of the catalytic activity. Here, we planned to test the HER and OER electrochemical properties of the uniform NPs decoration on the

highly porous NFs of the electrodes. The LSV measurements are presented in Figure 10A. The electrocatalytic activities of the porous NFs of NCO, NPs decorated NFs of NMCO4, and NSs of the MnCo_2O_4 electrodes were performed in the 1 M KOH electrolyte with 3-electrode measurements.⁵² The LSV curve shows that the catalytic activity of the optimized $\text{Ni}_{0.8}\text{Mn}_{0.2}\text{Co}_2\text{O}_4$ electrode is superior to other electrodes. The observed overpotential values of the NiCo_2O_4 , $\text{Ni}_{0.8}\text{Mn}_{0.2}\text{Co}_2\text{O}_4$, and MnCo_2O_4 electrodes are 176, 150, and 197 mV, at a constant current density of 10 mA cm⁻². To compare the superiority of optimized NiCo_2O_4 , $\text{Ni}_{0.8}\text{Mn}_{0.2}\text{Co}_2\text{O}_4$, and MnCo_2O_4 catalyst with commercial prepared Pt/C catalyst, the LSV curve of Pt/C as shown in Figure S8a.⁵³ The resultant values indicate the optimized $\text{Ni}_{0.8}\text{Mn}_{0.2}\text{Co}_2\text{O}_4$ electrode provided the lower values of the overpotential to others, as shown in Figure 10B.⁵² A comparative study with previously reported compounds with $\text{Ni}_{0.8}\text{Mn}_{0.2}\text{Co}_2\text{O}_4$ is

shown in Table S2. Wang et al.⁵⁴ prepared N-Ni₁Co₃Mn_{0.4}O/NF material by hydrothermal route for multifunctional electrocatalyst applications like HER, urea oxidation reaction, and hydrazine oxidation reaction. They reported that different molar ratio of the Ni and Co with 0.4 mM doping of the Mn, shows the more suitable material for the catalytic performance. They reported that the prepared N-Ni₁Co₃Mn_{0.4}O/NF electrode showed values overpotential (177 mV), and the Tafel slope (189 mV dec⁻¹), because of the larger active surface area. Similarly, Lan et al.⁵⁵ reported multiple applications of as-prepared In-doped MnCo₂O₄ material using a laser-assisted method for pseudocapacitors and HER. They synthesized the In-MnCo₂O₄ electrode deposited on Ni foam by the in-situ method. They reported the Cs of In-MnCo₂O₄ material of 1436.8 F g⁻¹ at 1 A g⁻¹ with poor cycling stability (71.9%). Also, they reported the electrocatalytic activity of the as-prepared In-MnCo₂O₄ catalyst, showing lower values of s the lower overpotential and a Tafel slope (76 mV dec⁻¹). Table S2 along with reported results, indicates the present value of overpotential for Ni_{0.8}Mn_{0.2}Co₂O₄ are much better than others.^{52,54} Because the present nanomaterials provide a higher surface area and shorter path length for ion diffusion which results in improved values of overpotential. These results indicate the chemically prepared quaternary Ni_{0.8}Mn_{0.2}Co₂O₄ nanomaterial is a better option than the other binary and ternary metal oxides.⁵²⁻⁵⁵ For a more detailed examination of the prepared electrodes, we obtained the Tafel slope of the prepared NiCo₂O₄, Ni_{0.8}Mn_{0.2}Co₂O₄, and MnCo₂O₄ electrodes shown in Figure 10C. The values of the Tafel slope indicate the optimized Ni_{0.8}Mn_{0.2}Co₂O₄ electrode shows a smaller Tafel slope (161 mV dec⁻¹) than the other two NCO (185 mV dec⁻¹) and MCO (214 mV dec⁻¹) electrodes (Table S2).⁵²⁻⁵⁶ The catalytic stability of the NCO, NMCO₄, and MCO catalyst was studied using chronopotentiometry for 10 hours, as shown in Figure 10D, the catalytic curve of the stability indicates the hybrid phase of Ni_{0.8}Mn_{0.2}Co₂O₄ catalyst superior to the NiCo₂O₄, MnCo₂O₄. The catalytic curve of the stability shows the Ni_{0.8}Mn_{0.2}Co₂O₄ electrode is more superior and capable electrocatalyst for HER application than the other ternary metal oxides. Figure S9a-c and Figure S10a-c show the surface morphology and XPS results of HER after the stability of the NiCo₂O₄, Ni_{0.8}Mn_{0.2}Co₂O₄, and MnCo₂O₄. The SEM clearly shows a small change in surface morphology was noticed. Similarly, XPS analysis indicates no large change in the chemical compositions after HER stability of NiCo₂O₄, Ni_{0.8}Mn_{0.2}Co₂O₄, and MnCo₂O₄ catalyst.

Additionally, we performed other applications of electrocatalytic activities for the OER, so we tested electrochemical performance in terms of LSV

measurements at 2 mV s⁻¹, in the 1 KOH electrolytes. The OER curves of the prepared NiCo₂O₄ (NCO), Ni_{0.8}Mn_{0.2}Co₂O₄ (NMCO₄), and MnCo₂O₄ (MCO) electrodes are presented in Figure 11A. The LSV curves of prepared NiCo₂O₄, Ni_{0.8}Mn_{0.2}Co₂O₄, and MnCo₂O₄ electrodes show the oxidation peaks observed at the range of 1.2 and 1.5 V vs RHE, which is attributed to different species of transition metals of Ni²⁺/Ni³⁺, Co²⁺/Co³⁺, and Mn²⁺ redox couple with the oxide elements.⁵³⁻⁵⁷ Figure S8b shows the commercial LSV curves of RuO₂ catalyst to compare the superiorities of the prepared materials.⁵³ Figure 11B shows the overpotential values of the as-prepared NiCo₂O₄, optimized Ni_{0.8}Mn_{0.2}Co₂O₄, and MnCo₂O₄ electrodes at a constant current density of 10 mA cm⁻². The Ni_{0.8}Mn_{0.2}Co₂O₄ electrode obtained values of the overpotential of 123 mV, which demonstrated higher catalytic activity than the other NiCo₂O₄ (341 mV) and MnCo₂O₄ (256 mV).

Rohit et al.⁵⁶ reported that ternary double-layer hydroxides material by a facile electrodeposition method at different molar ratios of Co-, Ni-, and Fe-based material for the multi-applications of supercapacitors and electrocatalysis. The electrochemical properties indicate that the Ni-rich electrode material shows more Cs (467 C g⁻¹) at a constant scan rate of 5 mV s⁻¹ than the Fe-rich, and Co-rich, respectively. Also, they reported that the Ni-rich layered double hydroxides electrode shows better cycling stability up to 2000 cycles. Furthermore, they reported that the Ni-rich electrode shows better electrocatalytic activity than the Co and Fe-rich material. They reported the overpotential of 139 mV and the Tafel slope (46 mV dec⁻¹) at the current density of 10 mA cm⁻², for Ni-rich. They concluded that the Ni-rich electrode shows superb electrocatalytic activity, because of the synergic effect between Co, Ni, and Fe and the more surface area. Sivakumar et al.⁵⁸ prepared NPs-like NiCoMnO₄ composite with different compositions by a simple hydrothermal route. The prepared composition was annealed at 600°C temperature in air atmospheric and used for the ORR and OER activities. They reported that the Ni_{1.5}Co_{0.75}Mn_{0.75}O₄ catalyst shows a low overpotential (180 mV) than the other materials. Finally, they concluded that the catalytic activity depends on the compositions of the Ni, Mn, and Co elements.⁵⁸ The obtained values of the overpotential of the OER are better than the previously reported, noticed in Table S3. Another important parameter of electrocatalytic activity is the Tafel slope, shown in Figure 11C. The Tafel slope of the optimized Ni_{0.8}Mn_{0.2}Co₂O₄ electrode was found to be 47 mV dec⁻¹, which is smaller than as-prepared NiCo₂O₄ (69 mV dec⁻¹) and MnCo₂O₄ (55 mV dec⁻¹).^{52,59-62} Figure 11D presents the catalytic stability of the NiCo₂O₄,

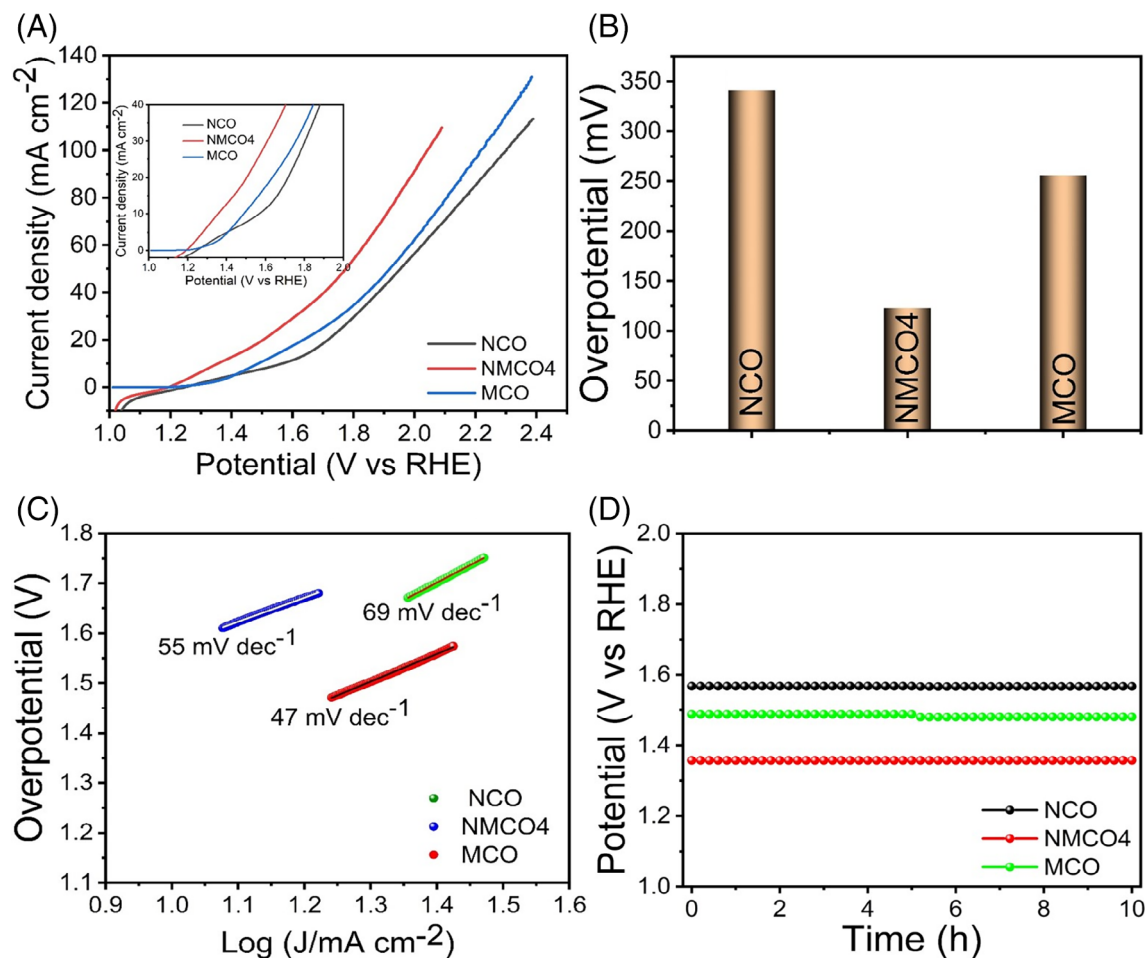


FIGURE 11 (A) OER electrochemical properties of NCO, NMCO4, and MCO electrodes in a 1 M KOH electrolyte, (B) Overpotential of the NCO, NMCO4, and MCO electrodes at constant current density 10 mA cm^{-2} , (C) Tafel slope of the NCO, NMCO4, and MCO electrodes, (D) Chronopotentiometric curves of NCO, NMCO4, and MCO electrodes for 10 h

$\text{Ni}_{0.8}\text{Mn}_{0.2}\text{Co}_2\text{O}_4$, and MnCo_2O_4 electrodes were studied at the constant current density of 10 mA cm^{-2} for 10 hours. These results indicate the hybrid $\text{Ni}_{0.8}\text{Mn}_{0.2}\text{Co}_2\text{O}_4$ material is more stable than the others.^{63,64} The comparative study shown in Table S3 indicates the hybrid $\text{Ni}_{0.8}\text{Mn}_{0.2}\text{Co}_2\text{O}_4$ material better electrocatalyst material for the OER activity. After the OER stability testing, SEM shows little damage in the surface morphological results (Figure S9d-f). Figure S10a-c shows the XPS results after the OER stability testing, which indicates no measurable change in the chemical and elemental composition. The HER and OER results demonstrated that the $\text{Ni}_{0.8}\text{Mn}_{0.2}\text{Co}_2\text{O}_4$ composite is a better electrode nano-material for excellent electrocatalytic activity and supercapacitor applications.⁵³⁻⁵⁵

For the outstanding catalytic activity of the HER and OER results, we carried out the electrochemically active surface area (ECSA) and electrochemical double-layer capacitance (C_{dl}) to deeply understand the relation between the surface area and electrochemical catalytic

activity. The electrochemical CV was tested in the non-faradaic area to obtain C_{dl} values. Figure S11a-c presents the CV results of the NiCo_2O_4 , $\text{Ni}_{0.8}\text{Mn}_{0.2}\text{Co}_2\text{O}_4$, and MnCo_2O_4 catalysts, respectively. Figure S11d represents the C_{dl} values of the NiCo_2O_4 , $\text{Ni}_{0.8}\text{Mn}_{0.2}\text{Co}_2\text{O}_4$, and MnCo_2O_4 catalysts, calculated through half of the slope.⁵³ The calculated values of C_{dl} show the higher values of the $\text{Ni}_{0.8}\text{Mn}_{0.2}\text{Co}_2\text{O}_4$ (1.56 mF cm^{-2}) as compared to the NiCo_2O_4 (0.78 mF cm^{-2}), and MnCo_2O_4 (0.56 mF cm^{-2}) catalyst, showing that $\text{Ni}_{0.8}\text{Mn}_{0.2}\text{Co}_2\text{O}_4$ offers the higher electrochemical active surface area and C_{dl} . The ECSA was calculated using the standard Equation.⁶⁵

$$ECSA = \frac{C_{dl}}{C_s}$$

where, C_{dl} is electrochemical double-layer capacitance, and C_s is the standard value of the ECSA ($C_s = 0.040 \text{ mF cm}^{-2}$).⁶⁶ The calculated values of ECSA are represented in the graphical, as shown in

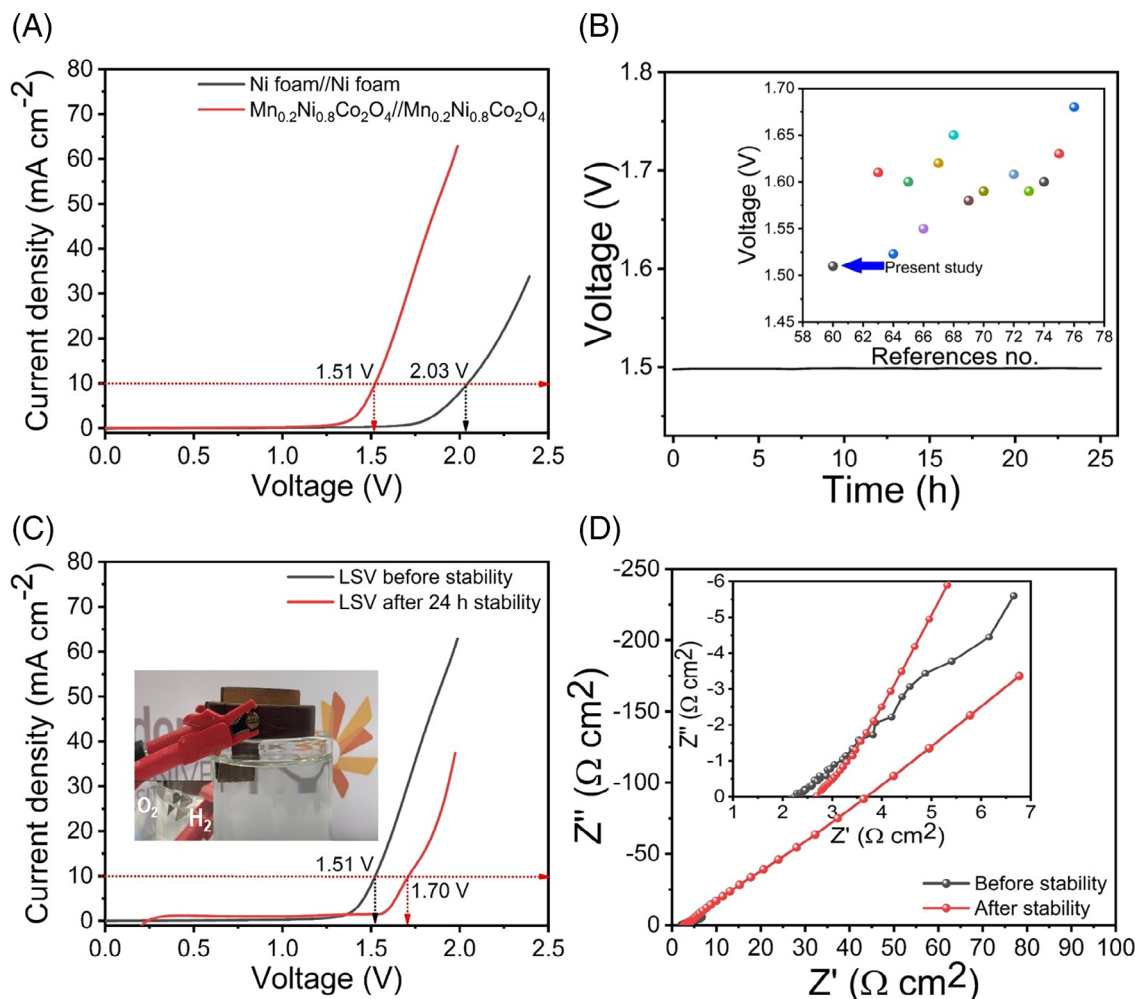


FIGURE 12 The catalytic measurements of the $\text{Ni}_{0.8}\text{Mn}_{0.2}\text{Co}_2\text{O}_4/\text{Ni}$ // $\text{Ni}_{0.8}\text{Mn}_{0.2}\text{Co}_2\text{O}_4/\text{Ni}$ for overall water splitting, (A) LSV of Ni//Ni foam, and $\text{Ni}_{0.8}\text{Mn}_{0.2}\text{Co}_2\text{O}_4/\text{Ni}$ // $\text{Ni}_{0.8}\text{Mn}_{0.2}\text{Co}_2\text{O}_4/\text{Ni}$ electrode, (B) stability testing up to 25 h, inset shows the comparative study with present results, (C) First, and last LSV cycles and inset show the real photographs of the overall water splitting activity its setup, and (D) Nyquist plots of after and before stability the assembled cell

Figure S11e. The ECSAs results show the quaternary $\text{Ni}_{0.8}\text{Mn}_{0.2}\text{Co}_2\text{O}_4$ catalyst is much more than the other, indicating the $\text{Ni}_{0.8}\text{Mn}_{0.2}\text{Co}_2\text{O}_4$ catalyst improves the electroactive area than the ternary NiCo_2O_4 , and MnCo_2O_4 .^{67–69} The LSV curves of NiCo_2O_4 , $\text{Ni}_{0.8}\text{Mn}_{0.2}\text{Co}_2\text{O}_4$, and MnCo_2O_4 electrodes are normalized by ECSA current, as shown in Figure S11f, Similar nature of the results are reported in the previous work.^{66,67} The specific activity was calculated from the electrochemical active surface area of the electrodes, presented in Figure S11f, and calculated values indicate the $\text{Ni}_{0.8}\text{Mn}_{0.2}\text{Co}_2\text{O}_4$ catalyst provided a larger catalytic performance than other electrodes.^{68–70} Furthermore, the TOF of all samples was calculated for HER activity using standard relation. The $\text{Ni}_{0.8}\text{Mn}_{0.2}\text{Co}_2\text{O}_4$ shows a TOF of 3.014 s^{-1} for HER activity. The details for TOF calculations are included in the supporting file [Section 2.5].

3.8 | Overall water splitting studies of $\text{Ni}_{0.8}\text{Mn}_{0.2}\text{Co}_2\text{O}_4/\text{Ni}$ // $\text{Ni}_{0.8}\text{Mn}_{0.2}\text{Co}_2\text{O}_4/\text{Ni}$ cells

Considering the outstanding HER and OER electrocatalysis performance of the optimized $\text{Ni}_{0.8}\text{Mn}_{0.2}\text{Co}_2\text{O}_4/\text{Ni}$ electrodes, we planned to use this electrode as a bifunctional electrocatalyst. The measurement for overall water splitting activity was carried out at room temperature (278 K) by considering $\text{Ni}_{0.8}\text{Mn}_{0.2}\text{Co}_2\text{O}_4/\text{Ni}$ electrode as both cathode and anode. Figure 12A presents LSV curves of the Ni//Ni and $\text{Ni}_{0.8}\text{Mn}_{0.2}\text{Co}_2\text{O}_4/\text{Ni}$ // $\text{Ni}_{0.8}\text{Mn}_{0.2}\text{Co}_2\text{O}_4/\text{Ni}$ cells. The LSV curves of Ni//Ni and $\text{Ni}_{0.8}\text{Mn}_{0.2}\text{Co}_2\text{O}_4/\text{Ni}$ // $\text{Ni}_{0.8}\text{Mn}_{0.2}\text{Co}_2\text{O}_4/\text{Ni}$ cells show a current density of 10 mA cm^{-2} at a potential of 2.03 V and 1.51 V, respectively. The present overall water splitting performance of the $\text{Ni}_{0.8}\text{Mn}_{0.2}\text{Co}_2\text{O}_4/\text{Ni}$ // $\text{Ni}_{0.8}\text{Mn}_{0.2}\text{Co}_2\text{O}_4/\text{Ni}$ cell was excellent when compared with the previously reported ternary NiCo_2O_4 and

MnCo₂O₄-based cells,⁷¹ for instance, Ni₅Mo/NiCo₂O₄/NF||Ni₅Mo/NiCo₂O₄/NF (1.54 V), and Ni₅Mo/NF||NiCo₂O₄/NF (1.61 V),⁷² FeP-NCO@NF (1.523 V),⁷³ Ru-NiCo₂O₄ (1.60 V),⁷⁴ Co₉S₈@NiCo₂O₄-70//Co₉S₈@NiCo₂O₄-10 cycles of (1.55 V),⁷⁵ MoS₂/NiCo₂O₄/NF (1.62 V),⁷⁶ NiCo₂O₄/NiCo₂O₄ (1.65 V),⁷⁷ NiCo₂O₄@Ni₂P/NAs (1.58 V),⁷⁸ NiCo₂O₄@NiWO₄/NF (1.59 V),⁷⁹ rGO-NiCo₂O₄ (1.5 V),⁸⁰ NiCo₂O₄@C//NiCo₂O₄@C (1.608 V),⁸¹ NiCo₂O₄ (1.59 V),⁸² NiCo₂O₄@NiMoO₄ (1.60),⁸³ Ar-NiCo₂O₄|S (1.63 V),⁸⁴ P-NiCo₂O₄/NF||P-NiCo₂O₄/NF (1.68 V),⁸⁵ etc. The overall water splitting results show superb activity due to the finer size of NPs (less than 5-10 nm) and the highly porous and ultrathin nanoflakes-like microstructure, providing faster pathways to the electron transfers. Furthermore, the stability testing of the Ni_{0.8}Mn_{0.2}Co₂O₄/Ni//Ni_{0.8}Mn_{0.2}Co₂O₄/Ni cell was studied by chronoamperometry technique as shown in Figure 12B. The long-term water-splitting performance depicts excellent durability of the electrocatalysts (up to 25 hours), which indicates the Ni_{0.8}Mn_{0.2}Co₂O₄ electrode is an efficient nanomaterial for the overall water-splitting application.⁸⁵

Figure 12C presented the LSV curves of the before and after stability tests of Ni_{0.8}Mn_{0.2}Co₂O₄/Ni//Ni_{0.8}Mn_{0.2}Co₂O₄/Ni cell, providing an overall water-splitting potential of 1.51 to 1.70 V, at the same current density of 10 mA cm⁻². The difference between the before and after stability is 0.19 V, which indicates the Ni_{0.8}Mn_{0.2}Co₂O₄ electrode is more stable as compared to the previously reported values.⁷²⁻⁷⁸ The EIS study of Ni_{0.8}Mn_{0.2}Co₂O₄/Ni//Ni_{0.8}Mn_{0.2}Co₂O₄/Ni cell shows the values of R_s and R_{ct} before and after stability testing, as shown in Figure 12D. The R_s and R_{ct} values indicate the assembled cell is more stable after 25 hours, which suggests the Ni_{0.8}Mn_{0.2}Co₂O₄ is the best electrocatalytic material for the efficient water splitting applications.⁸³⁻⁸⁵

4 | CONCLUSION

In conclusion, typical hybrid nanoparticle and ultrathin nanoflakes-like Ni_{1-x}Mn_xCo₂O₄ nanocomposites were successfully synthesized using a facile DES and drop coating method. The surface morphological results revealed that the change in the composition ratio of Ni and Mn significantly affected the surface morphology of the as-prepared Ni_{1-x}Mn_xCo₂O₄ hybrid nanostructures (X = 0, 0.2, 0.4, 0.6, 0.8, and 1). Furthermore, among the Ni_{1-x}Mn_xCo₂O₄ nanostructures, Ni_{0.8}Mn_{0.2}Co₂O₄ material exhibited the highest specific capacity (761 mAh g⁻¹ at 30 mA cm⁻²), which could be attributed to the uniform covering of the surface of the deposited 3D hierarchical vertically-grown nanoflakes with 1D NPs, which enhanced the electrical conductivity and Faradaic redox

reactions of the electrode. In addition, the cycling stability results revealed that the electrode exhibited an enhanced retention capacity of 92.86% after 10 000 cycles. Moreover, the solid-state hybrid device fabricated using the Ni_{0.8}Mn_{0.2}Co₂O₄ material exhibited a very high specific energy and specific power of 66.2 Wh kg⁻¹ and 1519 W kg⁻¹, respectively. Moreover, the NPs coated nanoflakes of the Ni_{0.8}Mn_{0.2}Co₂O₄ nanoelectrode exhibited a superb electrocatalytic activity for HER and OER in 1 M KOH electrolyte. These results indicate the promising potential of the double-layered TMO Ni_{1-x}Mn_xCo₂O₄ hybrid material as the electrode for the fabrication of industrial-level supercapacitors devices by advanced modification superb electrochemical activity of OER and HER are very useful for several fields in the markets. Furthermore, the assembly of the Ni_{0.8}Mn_{0.2}Co₂O₄/Ni//Ni_{0.8}Mn_{0.2}Co₂O₄/Ni cell provided a lower voltage of 1.51 V for overall water splitting activity with better durability after 25 hours. Moreover, the results revealed that the DSE method is a simple and useful method for tuning the morphology and electrochemical properties of electrodes and preparing novel quaternary hybrid nanomaterial for energy storage devices.

ACKNOWLEDGEMENTS

Analysis of samples was supported by Dongguk University, Seoul, and Korea Research Fund 2022-2024. ADJ is thankful to the Department of Science and Technology (DST), Govt. of India for financial assistance under the DST INSPIRE Faculty Scheme [DST/INSPIRE/04/2017/002737]. HMY acknowledges the Science & Engineering Research Board (SERB), a statutory body of the Department of Science & Technology (DST), Government of India for the award of the Ramanujan Fellowship (RJF/2020/000077).

ORCID

Surendra K. Shinde  <https://orcid.org/0000-0002-8630-8940>

Nagesh C. Maile  <https://orcid.org/0000-0002-6929-3791>

REFERENCES

1. Kamat PV. Lithium-Ion batteries and beyond: celebrating the Nobel prize in chemistry-a virtual issue. *ACS Energy Lett.* 2019; 4:2757-2759.
2. Lukatskaya MR, Dunn B, Gogosti Y. Multidimensional materials and device architectures for future hybrid energy storage. *Nat Commun.* 2016;7:12647.
3. Dubal DP, Chodankar NR, Kim DH, Gomez-Romero P. Towards flexible solid-state supercapacitors for smart and wearable electronics. *Chem Soc Rev.* 2018;47:2065-2129.
4. Chen GZ. Understanding supercapacitors based on nano-hybrid materials with interfacial conjugation. *Prog Nat Sci-Mater.* 2013;23:245-255.

5. Zhi M, Xiang C, Li J, Li M, Wu N. Nanostructured carbon-metal oxide composite electrodes for supercapacitors: a review. *Nanoscale*. 2013;5:72-88.
6. Lokhande CD, Dubal DP, Joo O-S. Metal oxide thin film based supercapacitors. *Curr Appl Phys*. 2011;11:255-270.
7. Lee W, Mane RS, Todkar VV, et al. Implication of liquid-phase deposited amorphous RuO₂ electrode for electrochemical supercapacitors. *Solid State Lett*. 2007;10:225.
8. Liu E-H, Meng X-Y, Ding R, Zhou J-C, Tan S-T. Potentiodynamical co-deposited manganese oxide/carbon composite for high capacitance electrochemical capacitors. *Mater Lett*. 2007;61:3486-3489.
9. Gund GS, Dubal DP, Shinde SS, Lokhande CD. Architected morphologies of chemically prepared NiO/MWCNTs Nanohybrid thin films for high-performance supercapacitors. *ACS Appl Mater Interfaces*. 2014;6:3176-3188.
10. Sankapal BR, Gajare HB, Karade SS, Dubal DP. Anchoring cobalt oxide nanoparticles on to the surface multiwalled carbon nanotubes for improved supercapacitive performances. *RSC Adv*. 2015;5:48426-48432.
11. Shelke AR, Lokhande AC, Pujari RB, Lokhande CD. Modification in supercapacitive behavior of CoO-rGO composite thin film from exposure to ferri/ferrocyanide redox-active couple. *J Colloid Interf Sci*. 2018;522:111-119.
12. Tajik S, Dubal DP, Gomez-Romero P, et al. Nanostructured mixed transition metal oxides for high performance asymmetric supercapacitors: facile synthetic strategy. *Int J Hydrogen Energ*. 2017;42:12384-12395.
13. Pettong T, Iamprasertkun P, Krittayavathananon A, et al. High-performance asymmetric supercapacitors of MnCo₂O₄ nanofibers and N-doped reduced graphene oxide aerogel. *ACS Appl Mater Interf*. 2016;8:34045-34053.
14. Dubal DP, Gomez-Romero P, Sankapal BR, Holze R. Nickel cobaltite as an emerging material for supercapacitors: An overview. *Nano Energy*. 2015;11:377-399.
15. Raut SS, Sankapal BR. Porous zinc cobaltite (ZnCo₂O₄) film by successive ionic layer adsorption and reaction towards solid-state symmetric supercapacitive device. *J Colloid Interface Sci*. 2017;487:201-208.
16. Karade SS, Lalwani S, Eum J-H, Kim H. Deep eutectic solvent-assisted synthesis of RuCo₂O₄: an efficient positive electrode for hybrid supercapacitors. *Sustainable Energ Fuel*. 2020;4:3066-3076.
17. Dubal DP, Chodankar NR, Holze R, Kim DH, Gomez-Romero P. Ultrathin mesoporous RuCo₂O₄ Nanoflakes: An advanced electrode for high-performance asymmetric supercapacitors. *ChemSusChem*. 2017;10:1771-1782.
18. Zhang Q, Vigier KDO, Royer S, Jerome F. Deep eutectic solvents: syntheses, properties and applications. *Chem Soc Rev*. 2012;41:7108-7146.
19. Tamboli MS, Dubal DP, Patil SS, et al. Mimics of microstructures of Ni substituted Mn_{1-x}Ni_xCo₂O₄ for high energy density asymmetric capacitors. *Chem Eng J*. 2017;307:300-310.
20. Jagadale AD, Rohit RC, Shinde SK, Kim D-Y. Materials development in hybrid zinc-ion capacitors. *ChemNanoMat*. 2021;7:1082-1098.
21. Shinde SK, Karade SS, Yadav HM, et al. Deep eutectic solvent mediated nanostructured copper oxide as a positive electrode material for hybrid supercapacitor device. *J Mol Liq*. 2021;341:117319.
22. Shinde SK, Ghodake GS, Maile NC, et al. Designing of nanoflakes anchored nanotubes-like MnCo₂S₄/halloysite composites for advanced battery like supercapacitor application. *Electrochim Acta*. 2020;341:135973.
23. Shinde SK, Jalak MB, Ghodake GS, et al. Chemically synthesized nanoflakes-like NiCo₂S₄ electrodes for high-performance supercapacitor application. *Appl Surf Sci*. 2019;466:822-829.
24. Shinde SK, Dubal DP, Ghodake GS, Fulari VJ. Hierarchical 3D-flower-like CuO nanostructure on copper foil for supercapacitors. *RSC Adv*. 2015;5:4443-4447.
25. Shinde SK, Dubal DP, Ghodake GS, Kim DY, Fulari VJ. Nanoflower-like CuO/cu(OH)₂ hybrid thin films: synthesis and electrochemical supercapacitive properties. *J Electroanal Chem*. 2014;732:80-85.
26. Shinde S, Dhaygude H, Kim D-Y, et al. Improved synthesis of copper oxide nanosheets and its application in development of supercapacitor and antimicrobial agents. *J Ind Eng Chem*. 2016;36:116-120.
27. Shinde SK, Kim D-Y, Ghodake GS, et al. Morphological enhancement to CuO nanostructures by electron beam irradiation for biocompatibility and electrochemical performance. *Ultrason Sonochem*. 2018;40:314-322.
28. Yadav HM, Ghodake GS, Kim D-Y, Sivalingam Ramesh NC, Maile DS, Lee SK. Shinde, Nanorods to hexagonal nanosheets of CuO-doped manganese oxide nanostructures for higher electrochemical supercapacitor performance. *Colloid Surface B*. 2019;184:110500.
29. Shinde SK, Yadav HM, Sivalingam R, et al. High-performance symmetric supercapacitor; nanoflower-like NiCo₂O₄/NiCo₂O₄ thin films synthesized by simple and highly stable chemical method. *J Mol Liq*. 2020;299:112119.
30. Kandula S, Raj Shrestha K, Rajeshkhanna G, Kim NH, Lee JH. Kirkendall growth and Ostwald ripening induced hierarchical morphology of Ni-co LDH/MMoS_x (M = co, Ni, and Zn) Heteronanostructures as advanced electrode materials for asymmetric solid-state supercapacitors. *ACS Appl Mater Interfaces*. 2019;11:11555-11567.
31. Zhao J, Chen J, Xu S, et al. Hierarchical NiMn layered double hydroxide/carbon nanotubes architecture with superb energy density for flexible supercapacitors. *Adv Funct Mater*. 2014;24:2938-2946.
32. Wang Y, Liu Y, Wang H, et al. Ultrathin NiCo-MOF Nanosheets for high-performance supercapacitor electrodes. *ACS Appl Energy Mater*. 2019;2:2063-2207.
33. Huang B, Wang W, Pu T, et al. Two-dimensional porous (co, Ni)-based monometallic hydroxides and bimetallic layered double hydroxides thin sheets with honeycomb-like nanostructure as positive electrode for high-performance hybrid supercapacitors. *J Coll Interf Sci*. 2018;532:630-640.
34. Padmanathan N, Selladurai S. Controlled growth of spinel NiCo₂O₄ nanostructures on carbon cloth as a superior electrode for supercapacitors. *RSC Adv*. 2014;4:8341-8349.
35. Maile NC, Moztahida M, Ghani AA, et al. Electrochemical synthesis of binder-free interconnected nanosheets of Mn-doped Co₃O₄ on Ni foam for high-performance electrochemical energy storage application. *Chem Eng J*. 2021;421:129767.
36. Xiao Y, Wei W, Zhang M, Jiao S, Shi Y, Ding S. Facile surface properties engineering of high-quality graphene: toward advanced Ni-MOF Heterostructures for high-performance,

- supercapacitor electrode. *ACS Appl Energy Mater.* 2019;2:2169-2177.
37. Sahoo S, Naik KK, Rout CS. Electrodeposition of spinel MnCo_2O_4 nanosheets for supercapacitor applications. *Nanotechnology.* 2015;26:455401-455409.
 38. Wan H, Liu J, Ruan Y, et al. Hierarchical configuration of NiCo_2S_4 nanotube@Ni-Mn layered double hydroxide arrays/three-dimensional graphene sponge as electrode materials for high-capacitance supercapacitors. *ACS Appl Mater Interfaces.* 2015;7:15840-15847.
 39. Yin C, Yang C, Jiang M, et al. A novel and facile one-pot Solvothermal synthesis of PEDOT-PSS/Ni-Mn-co-O hybrid as an advanced supercapacitor electrode material. *ACS Appl Mater Interfaces.* 2016;8:2741-2775.
 40. Mai LQ, Dong F, Xu X, et al. Cucumber-like $\text{V}_2\text{O}_5/\text{poly}(3,4\text{-ethyl-enedioxythiophene})$ & MnO_2 nanowires with enhanced electrochemical Cyclability. *Nano Lett.* 2013;13:740-745.
 41. Liu X, Shi C, Zhai C, Cheng M, Liu Q, Wang G. Cobalt based layered metal-organic framework as an ultrahigh capacity supercapacitor electrode material. *ACS Appl Mater Interfaces.* 2016;8:4585-4591.
 42. Li S, Huang W, Yang Y, et al. Hierarchical layer-by-layer porous $\text{FeCo}_2\text{S}_4/\text{Ni}(\text{OH})_2$ arrays for all-solid-state asymmetric supercapacitors. *J Mater Chem A.* 2016;6:20480-20490.
 43. Liu W, Niu H, Yang J, et al. Ternary transition metal sulfides embedded in graphene nanosheets as both the anode and cathode for high-performance asymmetric supercapacitors. *Chem Mater.* 2018;30:1055-1068.
 44. Zhao Y, Hu L, Zhao S, Wu L. Preparation of $\text{MnCo}_2\text{O}_4/\text{Ni}(\text{OH})_2$ Core-Shell flowers for asymmetric supercapacitor materials with ultrahigh specific capacitance. *Adv Funct Mater.* 2016;26:4085-4093.
 45. Chen WQ, Wang J, Ma KY, et al. Hierarchical $\text{NiCo}_2\text{O}_4/\text{Co-Fe}$ LDH core-shell nanowire arrays for high-performance supercapacitor. *Appl Surf Sci.* 2018;451:280-288.
 46. Lee H-M, CVV MG, Singh-Rana PJ, et al. Hierarchical nanostructured $\text{MnCo}_2\text{O}_4\text{-NiCo}_2\text{O}_4$ composite as an innovative electrode for supercapacitor applications. *New J Chem.* 2018;42:17190-17194.
 47. Chen H, Liu A, Mu J, Wu C, Zhang X. Template-free synthesis of novel flower-like MnCo_2O_4 hollow microspheres for application in supercapacitors. *Cer Int.* 2016;42:2416-2424.
 48. Cai N, Fu J, Chan V, et al. MnCo_2O_4 @nitrogen-doped carbon nanofiber composites with meso-microporous structure for high-performance symmetric supercapacitors. *J Alloys Comps.* 2019;782:251-262.
 49. Wang J, Sun M, Wang F, et al. Essential role of the interfacial interaction in the core-shell electrode for its enhanced electrochemical performance. *Chem Eng J.* 2021;426:130895.
 50. Ma D, Wang Y, Han X, Xu S, Wang J. Applicable tolerance evaluations of ion doped carbon nanotube/polypyrrole electrode under adverse solution conditions for capacitive deionization process. *Separ Purif Technol.* 2018;201:167-178.
 51. Chen X, He M, Zhou Y, et al. Design of hierarchical double-layer NiCo/NiMn-layered double hydroxide nanosheet arrays on Ni foam as electrodes for supercapacitors. *Mater Today Chem.* 2021;21:100507.
 52. Chu W, Shi Z, Hou Y, et al. Trifunctional of phosphorus-doped NiCo_2O_4 nanowire materials for asymmetric supercapacitor, oxygen evolution reaction, and hydrogen evolution reaction. *ACS Appl Mater Interfaces.* 2020;12:2763-2772.
 53. Mohite SV, Xing R, Li B, et al. Spatial compartmentalization of cobalt phosphide in P-doped dual carbon shells for efficient alkaline overall water splitting. *Inorg Chem.* 2020;59:1996-2004.
 54. Wang T, Cao Y, Huimin W, Chuanqi Feng Y, Ding HM. N-doped M/CoO (M=Ni, Co, and Mn) hybrid grown on nickel foam as efficient electrocatalyst for the chemical-assisted water electrolysis. *Int J Hydrogen Energ.* 2022;47:5766-5778.
 55. Lan B, Xiang Y, Luo X, et al. Charge regulation engineering to suppress Jahn-teller distortion in low crystallinity in-doping MnCo_2O_4 for high activity pseudocapacitors and hydrogen evolution reaction. *Chem Eng J.* 2022;430:132886.
 56. Rohit RC, Jagadale AD, Lee J, Lee K, Shinde SK, Kim D-Y. Tailoring the composition of ternary layered double hydroxides for supercapacitors and electrocatalysis. *Energ Fuel.* 2021;35:9660-9668.
 57. Gunjekar JL, Hou B, Inamdar AI, et al. Two-dimensional layered hydroxide nanoporous nanohybrids pillared with zero-dimensional polyoxovanadate nanoclusters for enhanced water oxidation catalysis. *Small.* 2018;14:1703481.
 58. Sivakumara P, Subramanian P, Maiyalagan T, Gedanken A. Ternary nickel single bond cobalt single bond manganese spinel oxide nanoparticles as heterogeneous electrocatalysts for oxygen evolution and oxygen reduction reaction. *Mat Chem Phys.* 2019;229:190-196.
 59. Rohit RC, Jagadale AD, Shinde SK, Kim D-Y, Kumbhar VS, Nakayama M. Hierarchical nanosheets of ternary CoNiFe layered double hydroxide for supercapacitors and oxygen evolution reaction. *J Alloy Compd.* 2021;863:158081.
 60. Deokate RJ, Mujawar SH, Chavan HS, et al. Chalcogenide nanocomposite electrodes grown by chemical etching of Ni-foam as electrocatalyst for efficient oxygen evolution reaction. *Int J Energ Res.* 2019;44:1233-1243.
 61. Liu Z, Tan H, Liu D, et al. Promotion of overall water splitting activity over a wide pH range by interfacial electrical effects of metallic niconitrides nanoparticle/ NiCo_2O_4 nanoflake/graphite fibers. *Adv Sci.* 2019;6:1801829.
 62. Zhou J-J, Kai XH, Li TQ, Li Y-L, Chen C, Han L. Shish-kebab type $\text{MnCo}_2\text{O}_4/\text{Co}_3\text{O}_4$ nanoneedle arrays derived from MnCoLDH@ZIF-67 for high-performance supercapacitors and efficient oxygen evolution reaction. *Chem Eng J.* 2018;354:875-884.
 63. Tahir M, Pan L, Zhang R, et al. High-valence-state NiO/ Co_3O_4 nanoparticles on nitrogen-doped carbon for oxygen evolution at low overpotential. *ACS Energy Lett.* 2017;2:2177-2182.
 64. Liu Z, Tan H, Liu D, et al. Promotion of overall water splitting activity over a wide pH range by interfacial electrical effects of metallic NiCo nitrides nanoparticle/ NiCo_2O_4 Nanoflake/graphite fibers. *Adv Sci.* 2019;6:1801829.
 65. Li Y, Zhao C. Enhancing water oxidation catalysis on a synergistic phosphorylated Nife hydroxide by adjusting catalyst wettability. *ACS Catal.* 2017;7:2535-2541.
 66. Santos HLS, Corradini PG, Medina M, Dias JA, Mascaro LH. NiMo-NiCu inexpensive composite with high activity for hydrogen evolution reaction, *ACS Appl. Mater. Interfaces.* 2020;12:17492-17501.

67. Sun QQ, Dong YJ, Wang ZL, Yin SW, Zhao C. Synergistic Nanotubular copper-doped nickel catalysts for hydrogen evolution reactions. *Small*. 2018;14:1704137.
68. Mahala C, Basu M. Nanosheets of NiCo₂O₄/NiO as efficient and stable Electrocatalyst for oxygen evolution reaction. *ACS Omega*. 2017;2:7559-7567.
69. Benson J, Li M, Wang S, Wang P, Papakonstantinou P. Electrocatalytic hydrogen evolution reaction on edges of a few-layer molybdenum disulfide Nanodots. *ACS Appl Mater Interfaces*. 2015;7:14113-14122.
70. McCrory CCL, Jung S, Peters JC, Jaramillo TF. Benchmarking heterogeneous Electrocatalysts for the oxygen evolution reaction. *J Am Chem Soc*. 2013;135:16977-16987.
71. Huang J, Wang S, Nie J, et al. Active site and intermediate modulation of 3D CoSe₂ nanosheet array on Ni foam by Mo doping for high-efficiency overall water splitting in alkaline media. *Chem Eng J*. 2021;417:128055.
72. Chen H, Qiao S, Yang J, Xiwen D. NiMo/ NiCo₂O₄ as synergy catalyst supported on nickel foam for efficient overall water splitting. *Mol Catalysis*. 2022;518:112086.
73. He B, Pan G, Deng Y, et al. Hierarchical iron-phosphide@ NiCo₂O₄ nanoneedle arrays for high-performance water splitting. *Appl Surf Sci*. 2021;569:151016.
74. Yang R, Shi X, Wang Y, et al. Ruthenium-modified porous NiCo₂O₄ nanosheets boost overall water splitting in alkaline solution. *Chinese Chem Lett*. 2021. doi:10.1016/j.ccl.2021.12.058
75. Du X, Zhang C, Wang H, Wang Y, Zhang X. Controlled synthesis of Co₉S₈@ NiCo₂O₄ nanorod arrays as binder-free electrodes for water splitting with impressive performance. *J of Alloy Compd*. 2021;885:160972.
76. Tao B, Yang L, Miao F, Zang Y, Chu PK. An MoS₂/NiCo₂O₄ composite supported on Ni foam as a bifunctional electrocatalyst for efficient overall water splitting. *J Phys Chem Solid*. 2021;150:109842.
77. Zhang L, Peng J, Zhang W, Yuan Y, Peng K. Rational introduction of borate and phosphate ions on NiCo₂O₄ surface for high-efficiency overall water splitting. *J Power Sources*. 2021;490:229541.
78. Wang Q, Wang H, Cheng X, et al. NiCo₂O₄@Ni₂P nanorods grown on nickel nanorod arrays as a bifunctional catalyst for efficient overall water splitting. *Mater Today Energ*. 2020;17:100490.
79. Du X, Shao Q, Zhang X. Metal tungstate dominated NiCo₂O₄ @NiWO₄ nanorods arrays as an efficient electrocatalyst for water splitting. *Int. J. Hydrogen Energ*. 2019;44(5):2883-2888.
80. Debata S, Patr S, Banerjee S, Madhuri R, Sharm PK. Controlled hydrothermal synthesis of graphene supported NiCo₂O₄ coral-like nanostructures: An efficient electrocatalyst for overall water splitting. *Appl Surf Sci*. 2018;449:203-212.
81. Deng J, Zhang H, Zhang Y, Luo P, Liu L, Wang Y. Striking hierarchical urchin-like peapodded NiCo₂O₄@C as an advanced bifunctional electrocatalyst for overall water splitting. *J Power Sources*. 2017;372(31):46-53.
82. Fang L, Jiang Z, Xu H, Liu L, Yongxinguan XG, Wang Y. Crystal-plane engineering of NiCo₂O₄ electrocatalysts towards efficient overall water splitting. *J Catal*. 2018;357:238-246.
83. Cui D, Zhao R, Dai J, Xiang J, Wu F. A hybrid NiCo₂O₄@Ni-MoO₄ structure for overall water splitting and excellent hybrid energy storage. *Dalton Trans*. 2020;49:9668-9679.
84. Lin JH, Yan YT, Qu TXXCQ, et al. S doped NiCo₂O₄ nanosheet arrays by Ar plasma: An efficient and bifunctional electrode for overall water splitting. *J Coll Interf Sci*. 2020;560:34-39.
85. Cheng L, Zhang R, Lv W, Shao L, Wang Z, Wang W. Surface Phosphation of 3D NiCo₂O₄ nanowires grown on Ni foam as an efficient bifunctional catalyst for water splitting. *Nano*. 2020;15:2050024.

SUPPORTING INFORMATION

Additional supporting information can be found online in the Supporting Information section at the end of this article.

How to cite this article: Shinde SK, Karade SS, Maile NC, et al. Bifunctional nanoparticles decorated Ni_{1-x}Mn_xCo₂O₄ ultrathin nanoflakes-like electrodes for supercapacitor and overall water splitting. *Int J Energy Res*. 2022;46(12):16693-16715. doi:10.1002/er.8333